Picosecond scale experimental verification of a globally convergent algorithm for a coefficient inverse problem

Michael V. Klibanov[*○], Michael A. Fiddy[◇△],
Larisa Beilina[**○], Natee Pantong[*○],   and John Schenk[◇△]
[*] Department of Mathematics and Statistics   [◇] Optoelectronics Center
[*◇] University of North Carolina at Charlotte, Charlotte, NC 28223, USA,
{mklibanv, mafiddy, npantong, schenk}@uncc.edu
[**] Department of Mathematical Sciences, Chalmers University
and Gothenburg University,   Gothenburg, Sweden, larisa@chalmers.se
[○] Mathematics sub-team. [△] Engineering sub-team

Abstract

A globally convergent algorithm of the first and third authors for a 3D hyperbolic coefficient inverse problem is verified on experimental data measured in the picosecond scale regime. Quantifiable images of dielectric abnormalities are obtained. The total measurement timing of a 100 pico-seconds pulse for one detector location was 1.2 nano-second with 20 pico-seconds (0.02 nano-second) time step between two consequtive readings. Blind tests have consistently demonstrated an accurate imaging of refractive indexes of dielectric abnormalities. At the same time, it is shown that a modified gradient method is inapplicable to this kind of experimental data. This inverse algorithm is also applicable to other types of imaging modalities, e.g. acoustics. Potential applications are in airport security, imaging of land mines, imaging of defects in non-distractive testing, etc..

1 Introduction

In recent publications [3, 4, 5, 6] of the first and third authors a new globally convergent numerical method for a Coefficient Inverse Problems (CIP) for a hyperbolic Partial Differential Equation (PDE) was developed analytically and tested numerically on computationally simulated data. The goal of the effort described in this publication was to verify the performance of that technique on a set of experimental data measured in the picosecond scale regime. The tomographic time resolved data were collected for the total timing of 12.3 nano-seconds per one detector location. Recall that 1 pico-second (ps)=10^{-12} second=10^3 nano-seconds

(ns). We present a radically new data processing procedure. The measured data were pre-processed by this procedure and were used then as Dirichlet boundary conditions for elliptic PDEs derived in [3, 4]. Next, images were obtained by the algorithm of [3, 4].

Only semi-blind data were used. Namely, it happen that we knew locations of dielectric inclusions, although this information is not used in our algorithm. However, we did not know values of refractive indexes of those inclusions. Therefore, we use the term *blind* everywhere below when talking about refractive indexes of inclusions used in experiments. After computational results were obtained, refractive indexes of inclusions were measured a posteriori by two well established methods. Comparison of measured and blindly computed refractive indexes has consistently demonstrated a very good accuracy of computed ones. It is an opinion of the authors that the latter fully verifies the technique of [3, 4, 5, 6].

We have obtained quantifiable non-destructive images of dielectric inclusions hidden in otherwise slowly changing background. "Quantifiable" means that the values of refractive indexes in those dielectric inclusions are accurately imaged. The accurate imaging of these values is an important ingredient in the goal of the identification of those abnormalities. Indeed, these values might help to differentiate between various types of dielectrics. Potential applications of the quantifiable imaging of dielectrics are in checking out baggages in airports, a stand-off detection of potential explosives hidden under clothing, imaging of antipersonnel land mines, etc.. Indeed, it is well known from, e.g. tables presented at http://www.clippercontrols.com/info/dielectric_constants.html# 1 that explosives have much higher dielectric constants than ones of regular materials. The framework of the technique of [3, 4] can be extended to the case when both the dielectric permittivity and the electric conductivity coefficients are unknown, although we have not worked out specific details yet.

In 2005 and 2009 Inverse Problems has published two special issues devoted to reconstructions of both dielectric and conductive abnormalities from experimental data [11, 18, 33, 34]. While the data of [33] of 2005 were designed for two-dimensional images, the data [34] of 2009 were collected for three-dimensional ones. These experimental data were provided by Fresnel Institute (Marseille, France). A number of good quality imaging results was published in these issues. We now list three main differences between our work and ones in [11, 18, 33, 34]:

1. Sources/Detectors Configurations. In our case only a single location of the source is used, and tomographic measurements are performed only on one side of a prism, which is opposite to the source location, see Figure 1 in section 5. Our source/detectors configuration uses the minimal amount of information. In addition, our source/detectors configuration can be easily transformed in the most interesting case (from the practical standpoint) of backscattering data, i.e. to the case of stand-off detection. The technique of [3, 4, 5, 6] can also be extended to this case [23]. In [33, 34] the source is moved all around the medium of interest and the data are collected all around a circle.

2. Convergence Analysis. The global convergence of our algorithm is rigorously guaranteed [3, 4], also see Theorem 1 in section 3. We work with a fully nonlinear problem and do not use neither a linearization, nor an assumption that the starting point is located close to the correct solution, nor an assumption about a priori knowledge of the background medium.

The only a priori knowledge we use is that the medium outside of our domain of interest is air and that the relative dielectric permittivity in the domain of our interest is not less than the one in the air, i.e. that the EM wave propagates in the domain of interest slower than in the air. In addition, it is shown in subsection 8.4 below that a modified gradient method cannot work for our experimental data. Works of [33, 34] use some variations of the small perturbation approach, e.g., Newton-like techniques. Convergence of the small perturbation approach cane be proven only under the condition that the starting point is located close to the correct solution.

3. Data Collection. We have measured the time resolved data generated by a 100 ps electric pulse. In [11, 18, 33, 34] the data are collected on several frequencies by the so-called Vector Network Analyzer technique. While formally measurements on several frequencies are equivalent with time resolved ones via the Fourier transform, it is the time resolved signal which provides the ultimate result.

We call a numerical method for a CIP *globally convergent* if the following two conditions are satisfied: (1) a theorem is proven, which ensures that this method provides a good approximation for the exact solution regardless on the availability of a good first guess for this solution, and (2) this analytical result is confirmed by numerical experiments. The fundamental underlying mathematical reason of the local convergence of conventional inverse algorithms is that CIPs are both nonlinear and ill-posed. It is because of the nonlinearity and ill-posedness that least squares residual functionals for CIPs suffer from multiple local minima and ravines, see, e.g. [21] for some examples. Therefore, any gradient-like method of minimization of such a functional likely stops at such a local minimum, which is the closest one to the starting point of iterations. Furthermore, because of the ill-posedness, there is no guarantee that a global minimum, even a well pronounced one, is close to the correct solution. The reason why we avoid the local minima problem is that our technique uses the structure of the underlying PDE operator instead of the least squares minimization.

Our technique is best suited for imaging of small inclusions. Another approach to imaging of small inclusions can be found in [2] and references cited there. Other procedures of solving CIPs, which do not rely on locally convergent algorithms, can be found in [9, 19, 20, 27, 28, 29]. In particular, techniques of [9, 20] work with CIPs for hyperbolic PDEs. We have cited only those techniques, which are numerically implemented: the method of [9] is implemented in [10], the method of [19, 28, 29] is implemented in [12] and works [20, 27] contain numerical studies. The main difference between these approaches and ours is in the nature of the information used. While these approaches use many locations of the source, we use a single source location.

This paper is organized as follows. In section 2 we formulate both forward and inverse problems of our mathematical model. In section 3 we outline the globally convergent numerical method of [3, 4], including both the formulation and a detailed discussion of the global convergence theorem. In section 4 we outline a modified gradient method for our CIP. In section 5 we describe the experimental set up. In section 6 we describe our data processing procedure. In section 7 we present some details of the numerical implementation of our algorithm. In section 8 results of numerical studies are presented. Discussion of results can

be found in section 9.

2   Forward and Inverse Problems

As the forward problem, we consider the following Cauchy problem

$$\varepsilon_r(x)u_{tt} \;\;=\;\; \Delta u, \text{ in } \mathbb{R}^3 \times (0,\infty), \tag{1}$$

$$u(x,0) \;\;=\;\; 0, u_t(x,0) = \delta(x-x_0). \tag{2}$$

Here $\varepsilon_r(x)$ is the spatially variable dielectric constant (relative dielectric permittivity),

$$\varepsilon_r(x) = \frac{\varepsilon(x)}{\varepsilon_0}, \sqrt{\varepsilon_r(x)} = n(x) = \frac{c_0}{c(x)}, \tag{3}$$

where ε_0 is the dielectric permittivity of the vacuum (which we assume to be the same as one in the air), $\varepsilon(x)$ is the spatially variable dielectric permittivity of the medium of interest, $n(x)$ is the spatially variable refractive index of the medium of interest, $c(x)$ is the speed of the propagation of the EM field in this medium, and c_0 is the speed of light in the vacuum, which we assume to be the same as one in the air. Thus, the refractive index shows how slower the EM field propagates in the medium of interest compared with the air. We assume below that $n(x) \geq 1$. We point out that equation (1) can be derived from the Maxwell's system only in two cases: (a) if $\varepsilon_r \equiv const. > 0$ and (b) in the 2-D case [13]. However, neither of these two is in place in our experiments. Thus, we call (1) a *simplified* mathematical model of our process. Currently we cannot explain why this model works for us and how it is compared with the performance of a model based on the full Maxwell's system.

Let $\Omega \subset \mathbb{R}^3$ be a convex bounded domain with the boundary $\partial\Omega \in C^3$. We assume that the coefficient $\varepsilon_r(x)$ of equation (1) is such that

$$\varepsilon_r(x) \;\;\geq\;\; 1, \varepsilon_r(x) = 1 \text{ for } x \in \mathbb{R}^3 \backslash \Omega, \tag{4}$$

$$\varepsilon_r(x) \;\;\in\;\; C^2\left(\mathbb{R}^3\right). \tag{5}$$

It is well known that the question of the existence of the fundamental solution (1), (2) is a very challenging one. Regardless on an extensive effort in the past of such people as J. Hadamard, S.L. Sobolev and V.G. Romanov, this question is currently positively addressed only under the condition that the coefficient $\varepsilon_r(x)$ is sufficiently smooth and geodesic lines generated by this coefficient are regular, see works of Romanov [31, 32] and citations of books J. Hadamard and S.L. Sobolev in them. Hence, it is inevitable that in the theoretical derivations of [3, 4] both (5) and the regularity of geodesic lines were assumed. Note that we need these assumptions only to make sure that the solution of the problem (1), (2) exists and that its Laplace transform (7) has a certain asymptotic behavior, see (16). However, we actually do not use these assumptions in our computational practice and verify (16) computationally, see subsection 7.2 in [3]. Likewise, although in our experiments the function

4

$\varepsilon_r(x)$ has a discontinuity at the boundary of a dielectric inclusion, which contradicts to (5), our reconstruction method still works.

Inverse Problem. *Suppose that the coefficient $\varepsilon_r(x)$ satisfies (4) and (5) and corresponding geodesic lines are regular. Assume that the function $\varepsilon_r(x)$ is unknown in the domain Ω. Determine the function $\varepsilon_r(x)$ for $x \in \Omega$, assuming that the following function $g(x,t)$ is known for a single source position $x_0 \notin \overline{\Omega}$*

$$u(x,t) = g(x,t), \forall (x,t) \in \partial\Omega \times (0,\infty). \tag{6}$$

In our application the assumption $\varepsilon_r(x) = 1$ for $x \in \mathbb{R}^3 \backslash \Omega$ means that one has air outside of the medium of interest Ω. The inequality $\varepsilon_r(x) \geq 1$ is because is that one should bound the coefficient $\varepsilon_r(x)$ from the below by a positive number to ensure that the operator in (1) is a hyperbolic one on all iterations of our numerical procedure. I addition this inequality means that the EM wave propagates slower in the domain of interest, compared with the air, see (3). The function $g(x,t)$ models time dependent measurements of the wave field at the boundary of the domain of interest. The question of uniqueness of this Inverse Problem is a well known long standing open problem. It is addressed positively only if the function $\delta(x - x_0)$ above is replaced with a such a function that $f(x) \neq 0, \forall x \in \overline{\Omega}$. Corresponding uniqueness theorems were proven via the method of Carleman estimates [21, 22], also, see a recent survey [36] on this method. It is an opinion of the authors that because of applications, it makes sense to develop numerical methods, assuming that the question of uniqueness of the above inverse problem is addressed positively.

3 Outline of the Globally Convergent Numerical Method

We outline in this section the method of [3, 4] as well as the global convergence theorem of [4], which is more advanced than one in [3]. We refer to these publications for details.

3.1 Outline

Consider the Laplace transform of the functions u,

$$w(x,s) = \int_0^\infty u(x,t)e^{-st}dt := \mathcal{L}(u), \text{ for } s > \underline{s} = const. > 0, \tag{7}$$

where $\underline{s}$ is a sufficiently large number such that the integral (7) converges together with corresponding (x,t)-derivatives. We call the parameter s *pseudo frequency*. Note that we do not use the inverse Laplace transform in our method, since approximations for the unknown coefficient are obtained in the pseudo frequency domain. We obtain from (1), (2)

$$\Delta w - s^2 c(x) w = -\delta(x - x_0), \tag{8}$$
$$\lim_{|x|\to\infty} w(x,s) = 0. \tag{9}$$

To prove (9), one can first consider a Laplace-like transform of the function $u(x,t)$ [26],

$$\widetilde{u}\left(x,t\right) = \frac{1}{2\sqrt{\pi}t^{3/2}} \int_0^{\infty} u(x,\tau) \exp\left(-\frac{\tau^2}{4t}\right) d\tau.$$

It was shown in [26] that the function $\widetilde{u}$ satisfies

$$\varepsilon_r\left(x\right)\widetilde{u}_t = \Delta\widetilde{u}, \widetilde{u}\left(x,0\right) = \delta\left(x - x_0\right). \tag{10}$$

Next, for sufficiently large s

$$w\left(x,s\right) = \int_0^{\infty} \widetilde{u}\left(x,t\right) \exp\left(-s^2 t\right) dt. \tag{11}$$

It follows from the classic estimate (6.13) of Chapter 4 of [25] for the fundamental solution of the parabolic PDE that the function $|\widetilde{u}|$ can be estimated from the above via the solution of another parabolic equation with constant coefficients. Finally, the Laplace transform (11) for the latter solution can be calculated via an explicit formula, and this formula implies decay as $|x| \to \infty$.

It follows from the classic theory of PDEs that for every $s > \underline{s}$ there exists unique solution $w \in C^{2+\alpha}\left(|x - x_0| \geq \gamma\right), \forall \gamma > 0$. Here and below $C^{k+\gamma}, \alpha \in \left(0,1\right), k \geq 0$, an integer, are Hölder spaces [24]. Since the fundamental solution $\widetilde{u}$ of the problem (10) is positive (Theorem 11 of Chapter 2 of [16]), then by (11) $w\left(x,s\right) > 0$ for sufficiently large $\underline{s}$ in (7). Hence, we can consider the function $v\left(x,s\right) = s^{-2}\ln w(x,s)$, which is the Liouville transform of the function w. The function v satisfies the following conditions

$$\Delta v + s^2\left(\nabla v\right)^2 = \varepsilon_r\left(x\right), x \in \Omega, \tag{12}$$
$$v \mid_{\partial\Omega} = \widetilde{\psi}\left(x,s\right),$$

where the function $\widetilde{\psi}$ is generated by the function g in (6). While (12) was obtained using the Liouville transform, a new step was proposed in [3]. The idea of this step has a root in the idea of applications of Carleman estimates to proofs of uniqueness theorems for CIPs [21, 22]. Namely, we eliminate the unknown coefficient $\varepsilon_r\left(x\right)$ from equation (12) via differentiating this equation with respect to s. Let $q\left(x,s\right) = \partial_s v\left(x,s\right)$. Then we obtain from (12) that the function $q\left(x,s\right)$ satisfies the following nonlinear integral differential PDE containing Volterra integrals with respect to s,

$$\Delta q - 2s^2 \nabla q \cdot \int_s^{\overline{s}} \nabla q\left(x,\tau\right) d\tau + 2s \left[\int_s^{\overline{s}} \nabla q\left(x,\tau\right) d\tau\right]^2$$

$$+ 2s^2 \nabla q \cdot \nabla V - 2s \nabla V \cdot \int_s^{\overline{s}} \nabla q\left(x,\tau\right) d\tau + 2s\left(\nabla V\right)^2 = 0, x \in \Omega, \tag{13}$$

$$q \mid_{\Omega} = \psi\left(x,s\right), \left(x,s\right) \in \partial\Omega \times \left[\underline{s},\overline{s}\right],$$

where $\psi(x,s) = \partial_s \widetilde{\psi}(x,s)$. Here $\overline{s}$ is the truncation pseudo frequency of integrals, which serves as one of regularization parameters of our method. Still, instead of just truncating the integral via setting its complement to zero, we use the function $V(x, \overline{s})$, which complements the rest of the integral, i.e.

$$v(x,s) = -\int_s^{\overline{s}} q(x,\tau)\, d\tau + V(x, \overline{s}), \tag{14}$$

$$V(x, \overline{s}) = v(x, \overline{s}) = \frac{\ln w(x, \overline{s})}{\overline{s}^2}. \tag{15}$$

We call $V(x, \overline{s})$ the "tail function", and it is unknown. Hence, equation (13) has two unknown functions, q and V. The reason why we can approximate well both of them is that we treat them differently. While we approximate the function q from inner iterations, the function V is approximated via outer iterations. In fact, numerical solution of the problem (13) is the *most challenging issue* in this method. It follows from (15) and Lemma 2.1 of [3], which is actually based on Theorem 4.1 of [31] as well as on the work [32] of the same author, that

$$\left\| \frac{\partial}{\partial s^k} V(x, \overline{s}) \right\|_{C^{2+\alpha}(\overline{\Omega})} = O\left(\frac{1}{\overline{s}^{k+1}} \right), \overline{s} \to \infty, k = 0, 1, ... \tag{16}$$

The problem (13) is solved via a layer stripping procedure with respect to the pseudo frequency s. Consider partition of the interval $[\underline{s}, \overline{s}]$ into N small subintervals of the width $h = s_{n-1} - s_n$, where $\underline{s} = s_N < s_{N-1} < ... < s_1 = \overline{s}$. Assume that $q(x,s)$ is a piecewise constant function with respect to s, $q(x,s) = q_n(x)$ for $x \in (s_n, s_{n-1}]$. Consider the Carleman Weight Function (CWF) $e^{\mu(s-s_{n-1})}$, where $\mu >> 1$ is a large parameter which should be chosen in computations. We multiply equation (13) by this function and integrate with respect to $s \in (s_n, s_{n-1})$. Hence, we obtain the Dirichlet boundary value problem for the following coupled system of nonlinear elliptic PDEs of the second order

$$L_n(q_n) \quad : \quad = \Delta q_n - A_{1,n}\left(h\sum_{i=1}^{n-1} \nabla q_i \right) \nabla q_n + A_{1n} \nabla q_n \nabla V - \varkappa q_n = B_n(\nabla q_n)^2$$

$$-A_{2,n}h^2\left(\sum_{i=1}^{n-1} \nabla q_i(x) \right)^2 + 2A_{2,n}\nabla V\left(h\sum_{i=1}^{n-1} \nabla q_i \right) - A_{2,n}(\nabla V)^2, \tag{17}$$

$$q_n \quad | \quad \partial\Omega = \psi_n(x) := \frac{1}{h}\int_{s_n}^{s_{n-1}} \psi(x,s)\, ds, \ n = 1, ..., N,$$

where the function $\psi(x,s)$ is taken from (13). In (17) $A_{1,n}, A_{2,n}, B_n$ are certain numbers depending on μ, h, n and $\varkappa > 0$ is a small parameter of ones choice. This parameter is introduced to obtain a better stability of the problem (17) because of the maximum principle, see §1 in Chapter 3 of [24]. It is important that $\lim_{\mu \to \infty} B_n = 0$ uniformly for all n due to the

presence of the CWF. Hence, the presence of the CWF with $\mu >> 1$ mitigates the influence of the nonlinear term $(\nabla q_n)^2$, which enables us to solve the boundary value problem for each q_n iteratively via solving a linear elliptic problem on each step. Still, the computational experience shows that we cannot take μ exceedingly large, which would effectively turn equations (17) into linear ones. Suppose that we have approximated the function $q_n(x)$. Then we find the approximation $\varepsilon_r^n(x)$ for the function $\varepsilon_r(x)$ via backwards calculation using (12) as

$$\varepsilon_r^{(n)}(x) = \begin{cases} f_n(x) := \Delta v_n + s_n^2 (\nabla v_n)^2, \ x \in \Omega, \ \text{if } f_n(x) \geq 1, \\ \quad\quad 1 \ \text{if } f_n(x) < 1, \end{cases} \tag{18a}$$

$$v_n(x) = -h \sum_{i=1}^{n} q_i(x) + V_n(x), \tag{18b}$$

where $V_n(x)$ is the corresponding approximation for the tail function. We make the cut-off to unity in (18a) because of (4).

Since the equation for each function q_n in (17) depends only on functions $q_1, ..., q_n$, then these elliptic Dirichlet boundary value problems can be solved sequentially: first one should approximate q_1, next approximate q_2, etc.. We have inner and outer iterations to solve these problems. While functions q_n are found from inner iterations, approximations for the tail function V are found from outer iterations. First, we choose the first approximation $V_{1,1}(x, \overline{s})$ for the tail function. In [3] $V_{1,1} \equiv 0$ was chosen. While we can still do so, we have discovered that the process converges faster if we choose the approximation, which corresponds to the case of the known value of the function $\varepsilon_r \equiv 1$ outside of the domain Ω. So, let $\widetilde{w}(x, \overline{s})$ be the solution of the problem (8), (9) with $\varepsilon_r \equiv 1$. Using (15), we set [4]

$$V_{1,1}(x) := \frac{\ln \widetilde{w}(x, \overline{s})}{\overline{s}^2}. \tag{19}$$

To approximate the function q_1, we first iterate with respect to the nonlinear term $(\nabla q_1)^2$ in (17) and find functions $q_1^k(x)$ this way setting in (17) $V := V_{1,1}$, where $V_{1,1}$ is defined in (19). So, we solve the Dirichlet boundary value problem (17) for functions $q_1^k(x)$ via setting for the nonlinear term $(\nabla q_n)^2 := (\nabla q_1^{k-1})^2$, $q_1^0 = 0$. We iterate with respect to the nonlinear term until convergence occurs. The resulting function is denoted as $q_{1,1}$.

For $n = 1$, we do not iterate with respect to the nonlinear term anymore. Instead, we iterate with respect to the tail as follows. Suppose we have obtained the pair $(q_{1,i}, V_{1,i})$. Then we find the approximation $\varepsilon_r^{(1,i)}(x)$ for the target coefficient $\varepsilon_r(x)$ via the backwards calculation (18a,b) with the obvious replacement of indexes. Next, we solve the problem (1), (2) with $\varepsilon_r := \varepsilon_r^{(1,i)}$, calculate the Laplace transform $w_{1,i+1}(x, s)$ of its solution and set the new approximation for the tail as $V_{1,i+1}(x) := \overline{s}^{-2} w_{1,i+1}(x, \overline{s})$. Next, we solve the boundary value problem (17) with $V := V_{1,i+1}, (\nabla q_n)^2 := (\nabla q_{1,i})^2$ and obtain the function $q_{1,i+1}$ this way. We continue this process until convergence occurs. Suppose that convergence occurs at $i := m_1$. Then we set $\left(q_1, \varepsilon_r^{(1)}, V_{2,1} \right) := \left(q_{1,m_1}, \varepsilon_r^{(1,m_1)}, V_{1,m_1} \right)$, for the nonlinear term in (17)

8

we set $(\nabla q_n)^2 := (\nabla q_2^0)^2 := (\nabla q_1)^2$. To find the function q_2, we repeat the above process for $n = 2$, etc., until convergence occurs. So, for each n we iterate with respect to the nonlinear term only to approximate $q_{n,1}$ and then we iterate with respect to tails. We can rigorously prove convergence of iterations with respect to the nonlinear term for each n (Theorem 1). However, we cannot prove convergence with respect to tails. Still, we have observed the latter numerically and our numerical convergence criteria are specified in subsection 7.1.

Since we have defined functions $\varepsilon_r^{(n,i)}$ in (18a,b) only for $x \in \Omega$, we explain now how we can extend these functions in $\mathbb{R}^3 \backslash \Omega$ in such a way that the resulting function belongs to $C^\alpha(\mathbb{R}^3)$. We need this explanation only for the sake of our global convergence theorem in the next subsection, since in the computational practice we just extend these functions as $\varepsilon_r^{(n,i)}(x) := 1$ for $x \in \mathbb{R}^3 \backslash \Omega$. Let $\Omega' \subset \Omega$ be a convex subdomain such that $dist(\partial\Omega', \partial\Omega) > 0$, where $dist(\partial\Omega', \partial\Omega)$ is the distance between these boundaries in the Hausdorf sense. We assume that the number $dist(\partial\Omega', \partial\Omega)$ is rather small, i.e. $\Omega' \approx \Omega$. It is well known from the Real Analysis course that one can choose such a function $\chi(x) \in C^\infty(\mathbb{R}^3)$ that

$$\chi(x) = \left\{ \begin{array}{c} 1 \text{ in } \Omega', \\ \text{between } 0 \text{ and } 1 \text{ in } \Omega \backslash \Omega', \\ 0 \text{ in } \mathbb{R}^3 \backslash \Omega. \end{array} \right.$$

So, suppose that in (18a,b) the function $\varepsilon_r^{(n,i)}(x) \in C^\alpha(\overline{\Omega})$. We define the function $\widehat{\varepsilon}_r^{(n,i)}(x)$ as $\widehat{\varepsilon}_r^{(n,i)}(x) = (1 - \chi(x)) + \chi(x)\varepsilon_r^{(n,i)}(x), \forall x \in \mathbb{R}^3$. Then $\widehat{\varepsilon}_r^{(n,i)} \in C^\alpha(\mathbb{R}^3), \widehat{\varepsilon}_r^{(n,i)} \geq 1, \widehat{\varepsilon}_r^{(n,i)}(x) = 1$ for $x \in \mathbb{R}^3 \backslash \Omega$ and $\widehat{\varepsilon}_r^{(n,i)}(x) = \varepsilon_r^{(n,i)}(x)$ in Ω'.

3.2 The global convergence theorem

To formulate this theorem, we need to introduce the definition of the exact solution first. We assume that there exists a coefficient $\varepsilon_r^*(x)$ satisfying condition (4), (5), and this function is an exact solution of our Inverse Problem with the "ideal" errorless data $g^*(x, t)$ in (6). The Laplace transform (7) of the function $g^*(x, t)$ leads to the exact function $\varphi^*(x, s) = w^*(x, s), \forall (x, s) \in \partial\Omega \times [\underline{s}, \overline{s}]$. Let

$$q^*(x, s) = \frac{\partial}{\partial s}\left[\frac{\ln[w^*(x, s)]}{s^2}\right], \quad V^*(x, \overline{s}) = \frac{\ln[w^*(x, \overline{s})]}{\overline{s}^2}.$$

Hence, $V^*(x, \overline{s})$ is the exact tail function. The function q^* satisfies an obvious analogue of equation (13) with the following boundary condition

$$q^*(x, s) = \psi^*(x, s) = \frac{1}{\varphi^* s^2}\frac{\partial\varphi^*}{\partial s} - \frac{2\ln\varphi^*}{s^3}, (x, s) \in \partial\Omega \times [\underline{s}, \overline{s}].$$

It easily follows from the above that the function $q^*(x, s) \in C^{2+\alpha}(\overline{\Omega}) \times C^\infty[\underline{s}, \overline{s}]$. First, we approximate functions $q^*(x, s)$ and $\psi^*(x, s)$ via piecewise constant functions with respect to $s \in [\underline{s}, \overline{s}]$ as

$$q_n^*(x) = \frac{1}{h}\int\limits_{s_n}^{s_{n-1}} q^*(x, s)\, ds, \quad \overline{\psi}_n^*(x) = \frac{1}{h}\int\limits_{s_n}^{s_{n-1}} \psi^*(x, s)\, ds. \tag{21}$$

9

Hence, for $n = 1, ..., N; s \in [s_n, s_{n-1}]$ we have $q^*(x,s) = q_n^*(x) + Q_n(x,s)$, $\psi^*(x,s) = \overline{\psi}_n^*(x) + \Psi_n(x,s)$, where functions Q_n, Ψ_n are such that $|Q_n(x,s)|_{2+\alpha} \leq C^*h$, $|\Psi_n(x,s)|_{2+\alpha} \leq C^*h$, for $s \in [s_n, s_{n-1}]$, where the constant $C^* = C^*\left(\|q^*\|_{C^{2+\alpha}(\overline{\Omega}) \times C^1[\underline{s},\overline{s}]}\right) > 0$ depends only on the $C^{2+\alpha}(\overline{\Omega}) \times C^1[\underline{s},\overline{s}]$ norm of the function $q^*(x,s)$. Here and below $|\cdot|_{k+\alpha}$ denotes the norm in the space $C^{k+\alpha}(\overline{\Omega})$. We can assume that

$$\max_{1 \leq n \leq N} |q_n^*|_{2+\alpha} \leq C^* \tag{22}$$

and without a loss of generality, we assume that

$$C^* \geq 1. \tag{23}$$

By the Tikhonov concept [35], the constant C^* should be known a priori. It is reasonable to assume that C^* is independent on $\overline{s}$, although we do not use this assumption. By (21) $q_n^*(x) = \overline{\psi}_n^*(x), x \in \partial\Omega$. We assume that the function $g(x,t)$ in (6) is given with an error. This naturally produces an error in the function $\psi(x,s)$ in (13). An additional error is introduced due to the averaging in (21). Hence, it is reasonable to assume that

$$\left\|\overline{\psi}_n^*(x) - \overline{\psi}_n(x)\right\|_{C^{2+\alpha}(\partial\Omega)} \leq C^*(\sigma + h), \tag{24}$$

where $\sigma > 0$ is a small parameter characterizing the level of the error in the data $\psi(x,s)$. We assume that

$$\overline{s} > 1, \; \lambda h \geq 1, \tag{25}$$

and introduce the positive constant $M^* = M^*\left(\|q^*\|_{C^{2+\alpha}(\overline{\Omega}) \times C^1[\underline{s},\overline{s}]}, \overline{s}\right) = M^*(C^*, \overline{s})$ by

$$M^* = 16C^*\overline{s}^2. \tag{26}$$

Consider the Dirichlet boundary value problem in the domain Ω

$$\Delta u + \sum_{j=1}^{3} b_j(x)u_{x_j} - d(x)u = p_1(x), \; u\mid_{\partial\Omega} = p_2(x) \in C^{2+\alpha}(\partial\Omega).$$

Assume that functions $b_j, d, p_1 \in C^\alpha(\overline{\Omega}), d(x) \geq 0$; $\max\left(|b_j|_\alpha, |d|_\alpha\right) \leq 1$. By the Schauder theorem [24], there exists unique solution $u \in C^{2+\alpha}(\overline{\Omega})$ of this boundary value problem, and with a constant $K = K(\Omega) > 1$, depending only on the domain Ω, the following estimate holds

$$|u|_{2+\alpha} \leq K\left[|p_1|_\alpha + \|p_2\|_{C^{2+\alpha}(\partial\Omega)}\right]. \tag{27}$$

Theorem 1 (global convergence) [4]. *Let $\Omega \subset R^3$ be a convex bounded domain with the boundary $\partial\Omega \in C^3$. Suppose that inequalities (22)-(25) hold. Let the exact coefficient $\varepsilon_r^*(x)$ satisfies conditions (4), (5). For any function $\varepsilon_r(x) \in C^\alpha(\mathbb{R}^3)$ such that $\varepsilon_r(x) \geq 1$ in Ω and $\varepsilon_r(x) = 1$ in $\mathbb{R}^3 \backslash \Omega$ consider the solution $u_{\varepsilon_r}(x,t)$ of the Cauchy problem (1), (2).*

Let $w_{\varepsilon_r}(x, s) \in C^{2+\alpha}(\{|x - x_0| \geq \gamma\}), \forall \gamma > 0$ be the Laplace transform (7) of $u_{\varepsilon_r}(x,t)$ and $V_{\varepsilon_r}(x) = \overline{s}^{-2} \ln w_{\varepsilon_r}(x, \overline{s}) \in C^{2+\alpha}(\overline{\Omega})$ be the corresponding tail function (see (15)). Suppose that the cut-off pseudo frequency $\overline{s}$ is so large that for any such function $\varepsilon_r(x)$ the following estimates hold

$$|V_{\varepsilon_r^*}|_{2+\alpha} \leq \xi, \quad |V_{\varepsilon_r}|_{2+\alpha} \leq \xi, \tag{28}$$

where $\xi \in (0, 1)$ is a sufficiently small number. Denote

$$\eta := 2(h + \sigma + \varkappa + \xi). \tag{29}$$

Let K be the constant of the Schauder theorem in (27) and $\overline{N} \leq N$ be the total number of functions q_n calculated by the algorithm of subsection 3.1. Suppose that the number $\overline{N} = \overline{N}(h)$ is connected with the step size h via $\overline{N}(h)h = \beta$, where the constant $\beta > 0$ is independent on h. Let β be so small that

$$\beta \leq \frac{1}{384K\overline{s}^2} = \frac{1}{24KM^*}. \tag{30}$$

In addition, let the number η and the parameter μ of the CWF satisfy the following estimates

$$\eta \leq \eta_0(K, C^*, \overline{s}) = \frac{1}{16KM^*} = \frac{1}{256KC^*\overline{s}^2}, \tag{31}$$

$$\mu \geq \mu_0(C^*, K, \overline{s}, \eta) = \max\left(\frac{(C^*)^2}{4}, 48KC^*\overline{s}^2, \frac{1}{\eta^2}\right).$$

Then for each $n \in [1, \overline{N}]$ the sequence $\{q_{n,1}^k\}_{k=1}^{\infty}$ converges in $C^{2+\alpha}(\overline{\Omega})$ to the function $q_{n,1}$. Likewise, if iterations of $\{q_{n,i}\}$ with respect to the tails are stopped at $i = m_n$ with $q_{n,m_n} := q_n$ for each $n \in [1, \overline{N}]$, then the following convergence estimates hold

$$|q_n - q_n^*|_{2+\alpha} \leq 2KM^*\left(\frac{1}{\sqrt{\mu}} + 3\eta\right), n \in [1, \overline{N}], \tag{32}$$

$$|q_n|_{2+\alpha} \leq 2C^*, \ n \in [1, \overline{N}],$$

$$\left|\varepsilon_r^{(n)} - \varepsilon_r^*\right|_{\alpha} \leq \frac{\eta}{2 \cdot 9^{n-1}} + \frac{23}{8}\eta, \ n \in [2, \overline{N}]. \tag{33}$$

3.3 Discussion of Theorem 1

3.3.1 The parameter ξ

By (16) and (28) the parameter ξ is small as long as the truncated pseudo frequency $\overline{s}$ is large. This implies of course that the parameter η in (29) is also small. Nevertheless, this theorem has a discrepancy related to the parameter ξ. Indeed, by (31) we should have $\eta \leq C_1/\overline{s}^2, C_1 = (256KC^*)^{-1}$. On the other hand, (16) implies that $\xi = O(1/\overline{s}), \overline{s} \to \infty$. Clearly these two conditions imposed on η and ξ are incompatible with (29). In addition

11

since by (26) $M^* = O(\bar{s}^2)$ as $\bar{s} \to \infty$, then there is no guarantee that the right hand side of (32) is small indeed.

We explain this discrepancy as follows. Since the problem of construction of globally convergent numerical methods for our CIP is obviously an extremely challenging one, we need to make certain compromises such as, e.g. ones outlined in the previous paragraph. In simple terms, not everything can be covered by the theory. The only way to justify these compromises is via numerical experiments. Numerical experiments of previous publications on this method [3, 4, 5, 6] fully confirm the theory, see, e.g. subsection 9.3 in [4]. Thus, they demonstrate that this compromise is reasonable. Note that we truncate our pseudo frequency "gently". In other words, instead of just setting for the tail function to be zero, we iterate with respect to tails. In addition, we refer to the Gelfand-Krein-Levitan method for a 2-D inverse hyperbolic problem of [20]. This method shows an excellent numerical performance. Still, it has a similar problem with the truncation of the Fourier series with respect to one of spatial variables. In connection with this compromise, we present a new mathematical model in the next sub-subsection and we also demonstrate that a very similar problem takes place in the classic Real Analysis. Finally, we believe that results of the current publication eliminate last remaining doubts about the validity of the technique of [3, 4], see section 9.

3.3.2 A new mathematical model and a classic example from Real Analysis

We associate with Theorem 1 a new mathematical model. In this model, as soon as the large truncation pseudo frequency $\bar{s}$ is chosen, we allow the parameter ξ, which bounds tails in (28) and which is involved in the convergence parameter η in (29), to be infinitely small, *independently* on $\bar{s}$. Actually, we do exactly this in our numerical implementation, which justifies this new model, see subsections 7.1 and 7.2 for details.

Finally, we provide here an example of the same nature. This example is linked with the classic issue of Asymptotic Series. Although these series quite often formally diverge, still their truncations provide very good approximations for corresponding functions. Consider the classic error function $\Phi(x)$ [1],

$$\Phi(x) = \frac{2}{\sqrt{\pi}} \int\limits_x^\infty e^{-t^2} dt, \ x > 0.$$

The asymptotic series expansion for the function $e^{x^2}\Phi(x)$ is

$$e^{x^2}\Phi(x) = \frac{1}{\sqrt{\pi}x}\left(1 + \sum_{n=1}^\infty (-1)^n \frac{(2n-1)!!}{(2x^2)^n}\right), x \to \infty,$$

where $(2n-1)!! = 1 \cdot 3 \cdot 5 \ldots \cdot (2n-1)$. This asymptotic series diverges for any x. Nevertheless, it is well known that the following is a good approximation for the function $e^{x^2}\Phi(x)$ for large values of x,

$$e^{x^2}\Phi(x) \approx \frac{1}{\sqrt{\pi}x}\sum_{n=1}^N (-1)^n \frac{(2n-1)!!}{(2x^2)^n}, x \to \infty.$$

The truncation number N here has exactly the same nature as our truncation pseudo frequency $\overline{s}$. Hence, this example demonstrates that things, which are similar to ours, exist in the classic Real Analysis, and they are related to the asymptotic series expansions.

3.3.3 The meaning of estimates (30) and (33)

The estimate (33) tells one that the accuracy of the reconstruction of the function ε_r^* is improving with iterations for the first few iterations. However, when n becomes sufficiently large, the norm $\left| \varepsilon_r^{(n)} - \varepsilon_r^* \right|_\alpha$ becomes comparable with the level of error $(23/8)\,\eta$. This error includes the error ξ in our new mathematical model, the error σ in the data and some less significant errors h and $\varkappa$ of our method. In other words, we cannot guarantee that our accuracy will improve after reaching a certain $n := n_0 \in \left[2, \overline{N} \right]$. In addition, by (30) we also cannot guarantee anything for $n > \overline{N}$. We indeed observe this in our computations, in which we take either $\overline{N} = 6$ or $\overline{N} = 5$, and we do this for a very plausible reason, see (49) and subsection 8.2 below. It was pointed out on pages 156 and 157 of the book [14] that one of backbone ideas of the theory of Ill-Posed Problems is to use the number of iterations as one of regularization parameters. This iteration number is $\overline{N}$ in our case. The true reason why the number β is small in (30) is that equations (17) are generated by equations (13), which contain nonlinear terms with Volterra integrals. It is well known that one can guarantee existence of solution of a nonlinear Volterra integral equation only on a small interval. For example, the Cauchy problem $y' = y^2 + 1, y(0) = 0$ has its solution $y(z) = \tan z$ with the singularity at $z = \pi/2$. On the other hand, this Cauchy problem is equivalent with the following nonlinear integral equation of the Volterra type

$$y(z) = \int_0^z y^2(\tau)\, d\tau + z.$$

4 A Modified Gradient Method

We use the method of this section for comparison with the globally convergent technique. Since the gradient method is a secondary to us and since we want to save space, we derive a modified gradient method only briefly here. First, we need is to introduce the Tikhonov functional for the above CIP in the pseudo frequency domain and derive its Frechét derivative. We call our technique of this section the "modified gradient method" because instead of making usual steps in the gradient method, we find the zero of the Frechét derivative of the Tikhonov functional via solving an equation with a contractual mapping operator. Our derivation of the Frechét derivative of the Tikhonov functional is similar with the derivation of [5] for the same CIP in the time domain. And so we refer to sections 6 and 7 of [5] for a similar and rigorous framework.

Let $\widetilde{g}(x, s)$ be the Laplace transform (7) of the function $g(x, t)$ in (6). Then

$$w(x, s)\, |_{\partial\Omega} = \widetilde{g}(x, s). \tag{34}$$

Since by (3) the coefficient $\varepsilon_r(x) = 1$ outside of Ω, then we can uniquely solve the boundary value problem (8), (9), (34) in the domain $\mathbb{R}^3 \backslash \Omega$ for every value of s of our interest. Hence, we can uniquely find the normal derivative $p(x,s) = \partial_n w(x,s)\mid_{\partial\Omega}$. Hence, we obtain the so-called "state" boundary value problem for the function w inside of the domain Ω,

$$
\begin{aligned}
\Delta w - s^2 \varepsilon_r(x)\, w &= 0 \text{ in } \Omega, \\
\partial_n w(x,s) \mid_{\partial\Omega} &= p(x,s).
\end{aligned}
\tag{35}
$$

In addition, consider the so-called "adjoint" boundary value problem for the function λ,

$$
\begin{aligned}
\Delta\lambda - s^2 \varepsilon_r(x)\,\lambda &= 0 \text{ in } \Omega, \\
\partial_n\lambda(x,s) \mid_{\partial\Omega} &= (w\mid_{\partial\Omega} -\widetilde{g})(x,s).
\end{aligned}
\tag{36}
$$

The idea of the gradient method is to find a zero of the Frechét derivative of the Tikhonov functional with the regularization parameter θ,

$$
E(\varepsilon_r) = \frac{1}{2}\int\limits_{c_1}^{c_2}\int\limits_{\partial\Omega}(w\mid_{\partial\Omega} -\widetilde{g})^2\, d\sigma_x ds + \frac{\theta}{2}\int\limits_{\Omega}\left(\varepsilon_r(x) - \varepsilon_r^{(0)}(x)\right)^2 dx,
$$

where (c_1, c_2) is an interval of pseudo frequencies, $w = w(x, \varepsilon_r)$ is the solution of the problem (35) and $\varepsilon_r^{(0)}$ is a first approximation for the unknown coefficient ε_r. In order to simplify the derivation of the Frechét derivative of this functional, consider the associated Lagrangian $L(\varepsilon_r)$,

$$
L(\varepsilon_r) = E(\varepsilon_r) + \int\limits_{c_1}^{c_2}\int\limits_{\partial\Omega} p\lambda\, d\sigma_x ds - \int\limits_{c_1}^{c_2}\int\limits_{\Omega}\left(\nabla w \nabla \lambda + s^2 \varepsilon_r(x) w\lambda\right) dx ds.
\tag{37}
$$

It follows from the definition of the weak solution of the problem (35) that the integral term in (37) equals zero. Hence, $L(\varepsilon_r) = E(\varepsilon_r)$ for all admissible functions $\varepsilon_r(x)$. This implies that $L'(\varepsilon_r) = E'(\varepsilon_r)$, where L' and E' are Frechét derivatives. To figure out the Frechét derivative $L'(\varepsilon_r)$, we need to vary in (37) the function ε_r via considering the function $\varepsilon_r(x) + b(x)$, where the functions $b(x)$ is an appropriate small perturbation of the function $\varepsilon_r(x)$. But since functions $w = w(x,s,\varepsilon_r)$ and $\lambda = \lambda(x,s,\varepsilon_r)$ depend on ε_r as solutions of boundary value problems (35) and (36), then we should also consider respective variations of these functions. In other words, we should consider Frechét derivatives of functions $w(x,s,\varepsilon_r), \lambda(x,s,\varepsilon_r)$ with respect to ε_r. These Frechét derivatives are actually solutions of such boundary value problems, which are obtained via the linearization of problems (35) and (36) with respect to b. Finally, the linear, with respect to $b(x)$, part of the difference $L(\varepsilon_r + b) - L(\varepsilon_r)$ is $L'(\varepsilon_r)(b)$. Again, the necessary formalism for the hyperbolic case can be found in [5], and our elliptic case is similar. So, finally we obtain

$$
E'(\varepsilon_r) = \theta\left(\varepsilon_r - \varepsilon_r^{(0)}\right)(x) - \int\limits_{c_1}^{c_2} s^2\, (w\lambda)(x,s,\varepsilon_r)\, ds.
$$

14

At a point of a minimum of the functional $E(\varepsilon_r)$ one should have $E'(\varepsilon_r) = 0$. Therefore, we should solve the following equation

$$\varepsilon_r(x) = \frac{1}{\theta} \int_{c_1}^{c_2} s^2 (w\lambda)(x, s, \varepsilon_r)\, ds + \varepsilon_r^{(0)}(x),\, x \in \Omega. \tag{38}$$

One can easily prove that one can choose the number $\zeta = (c_2 - c_1)/\theta$ so small that the equation (38) becomes an equation with the contraction mapping operator, which, therefore, can be solved iteratively. Of course, the number ζ should not be too small, since otherwise the resulting solution would be too close to the initial guess $\varepsilon_r^{(0)}$. So, one should choose optimal parameters c_1, c_2, θ.

5   Experimental Setup

5.1   Data acquisition
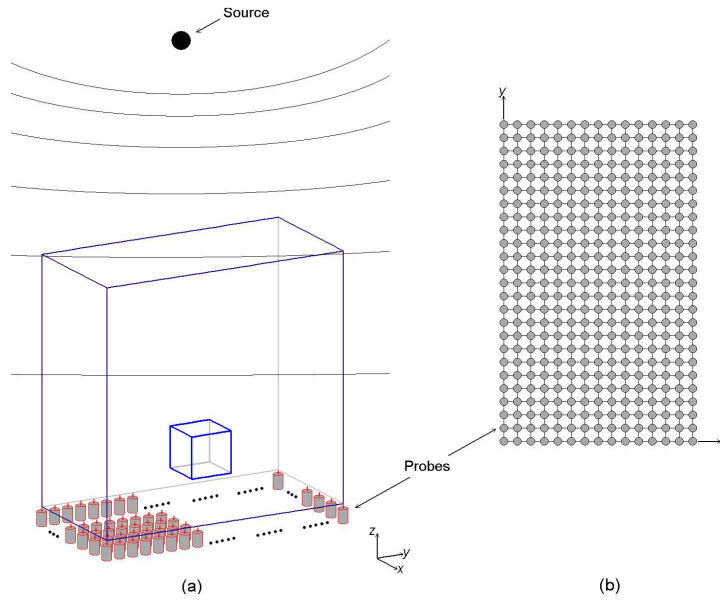
Figure 1. *Schematic diagram of the source/detectors configuration. a) The prism depicts our computational domain Ω. This domain is a part of another prism, which was our holder made out of Styrofoam. Only a single source location was used. Tomographic measurements of the scattered time resolved EM wave were conducted on the bottom side of this prism. b) Schematic diagram of locations of detectors (probes) on the bottom side of the prism Ω. The distance between neighboring probes was 10 mm.*

For brevity below x denotes both a vector $x \in \mathbb{R}^3$ and one of components of this vector $x = (x, y, z)$. It is always clear from the context what is what there. Our source/detectors configuration is schematically depicted on Figure 1. The source has generated an electromagnetic (EM) wave, which we wanted to be a plane wave when reaching the bottom side of the prism of Figure 1, where measurements were conducted. But actually this was a spherical wave, because of a rather small distance between the source and that side. We had a holder consisting of Styrofoam. Styrofoam is a material, whose relative permittivity $\varepsilon_r \approx 1$, i.e. the same as one in the air. Sizes of the holder were 260 mm×135 mm×260 mm. However, because of our previous computational experience [4], we have chosen another prism as our computational domain Ω, which mostly a part of this holder, except that its size in the y-direction was 5 mm more. It should be kept in mind that the above holder physically existed, whereas Ω was sort of "imaginary" domain which we have used for our computations. So sizes of the prism Ω were 240 mm×140 mm×240 mm. Hence, sizes of front and back sides of the prism of Figure 1 are 240 mm×240 mm, sizes of other four sides are 240 mm×140 mm, and this prism is exactly our domain Ω in (4). The distance between the wave source and the top side of the domain Ω was 130 mm. The initializing pulse was 100 ps duration. Since the speed of the EM wave propagation in the air is 0.3 mm/ps, then it requires 433 ps≈130/03 ps for this wave to travel form the source to the top boundary of Ω. Hence, the wave did not yet reach the prism Ω during the 100 ps duration of this pulse. The initializing pulse was

$$f(t) = \begin{cases} \approx A \sin\left(\frac{\pi}{50}\tau\right), \text{ for } \tau \in (0, 100) \text{ ps,} \\ \quad\quad 0, \text{ for } \tau > 100 \text{ ps,} \end{cases} \tag{39}$$

where A is the amplitude. Note that it is unclear a priori on how the value of A will be "reflected" in our mathematical model. Still, our data processing procedure does not rely on a knowledge of A. The time resolved signal was measured at some locations of the probe (i.e., detector) on the bottom side of the prism Ω, as indicated on Figure 1-b).

A special question to address was about the timing of measurements. The original pulse needs a few nanoseconds to go through the device and reach the tip of the EM wave generator, which is depicted on Figure 1 as the source location. In our mathematical model the zero time is the moment when the pulse leaves the tip of the generator. On the other hand, on each location of the probe measurements were conducted from the moment when the pulse was initiated "within" the device, which is prior the moment when it leaves the tip of the generator. Hence, actual measurements were conducted for times $\tau \in (0, 12300)$ ps $= (0, 12.3)$ ns, where τ is the real time with dimensions. We had two measurements at each probe location: (1) First we have measured the reference signal when the inclusion was not present, and (2) Second, we have measured the signal when the inclusion was present.

The step size in time between two consecutive measurements was $\Delta\tau = 20$ ps. Hence, we had only five (5) measurement points per 100 ps duration of the initializing pulse. This means that the sinusoidal behavior (39) is only an approximation of course. We have measured the scattering EM wave sequentially. In other words, first, we were putting the probe at one location, sent the pulse and measured the time resolved scattering wave at this location. Next, we

moved the probe mechanically in a neighboring location and repeated the measurement, etc.. The distance between two neighboring probe locations was 10 mm, and so we have covered the entire bottom side of the holder by this grid with 10 mm step size. Pulses were generated by the Picosecond Pulse Generator 10070A, see http://www.picosecond.com/. The scattered EM wave was measured by Tektronix DSA70000 Series Real Time Oscilloscope, see Tektronix, http://www.tek.com/products/oscilloscopes/.

a)   b)

Figure 2. *a) Picosecond Pulse Generator 10070A and b) Tektronix DSA70000 Series Real Time Oscilloscope*

5.2   Dimensionless variables

To work with the data, we have re-scaled our dimensions in time and space and have made them dimensionless. First, we have re-scaled spatial variables. While working previously with the above CIP for computationally simulated data [4] when the domain Ω was a prism with ratios of lengths of sides similar with ones of Figure 1, we have discovered that the step size $\widetilde{h} = 0.2$ when solving both forward and inverse problems was an optimal one. On the other hand, since we had the 10 mm distance between neighboring positions of the probe, we have decided to re-scale spatial variables in such a way that 10 mm would turn into 0.2 in dimensionless variables. So, let (x', y', z') be spatial variables with dimensions. Then, since $10/02=50$, we set for re-scaled dimensionless variables $(x, y, z) = (x', y', z') /50$. Thus, our dimensionless computational domain Ω for the CIP is

$$\Omega = \{(x, y, z) \in [-2.4, 2.4] \times [-1.4, -1.4] \times [-2.4, 2.4]\}. \tag{40}$$

Denote P the bottom side of the domain Ω in (40),

$$P = \{(x, y, z) : (x, y) \in [-2.4, 2.4] \times [-1.4, -1.4], z = -2.4\}. \tag{41}$$

We now should address the question on how long we should measure the scattered EM wave on probes located on P. It was not easy to find out in our experimental arrangement when exactly the pulse leaves the tip of the EM waves generator, i.e. the source depicted on Figure 1. However, we knew that the signal arrives at the probe approximately at 11,520

ps. Since the distance between the planar surface P and the source was 370 mm, the speed of light in the air is 0.3 mm/ps and $(370mm)/(0.3mm/ps) = 1233$ ps, then the zero time should be at $11,520$ ps$-1,233$ ps $\approx 10,300$ ps:$= \tau_0$. So, we should work with a new variable $\tau' = \tau - \tau_0$. The next question was on how to re-scale the time τ'. It follows from (1), (3) and (4) that the refractive index outside of the domain Ω is $n(x) = 1$. This means that the EM wave should travel the dimensionless distance of $\widetilde{h} = 0.2$ in 0.2 dimensionless time units. On the other hand, 0.2 corresponds to 10 mm. Let t denotes the dimensionless time. Then we should choose such a multiplier $\gamma > 0$ (γ has dimension in picoseconds) that $\gamma t = \tau'$. Hence, we should have $0.2 \gamma ps = 10mm/(0.3mm/ps)$, which implies that $\gamma = 166.67$ ps. Thus,

$$\gamma t = \tau', \gamma = 166.67 \text{ ps.} \tag{42}$$

Finally, we should figure out on how long we should measure the output signal. In [4] we have worked with the time interval $t \in (0,T) = (0,12)$. Since by (42) $12\gamma \approx 2000$ ps, then we should work with $\tau' \in (0,2000)$ ps. So, since by the above $\tau_0 = 10,300$ ps and $\tau' = \tau - \tau_0$, then the maximal value of τ of our interest is $12,300$ ps $= 10,300$ ps $+2000$ ps. Hence, we should measure the output signal for $\tau \in (0,12300)$ ps $= (0,12.3)$ ns.

Remark 5.1. When re-scaling in this sub-subsection, we have not reflected this in the corresponding PDE. This becomes possible because of the data processing procedure described in section 6. Below we work only with dimensionless time and spatial variables.

5.3 Why measuring the reference signal at each probe location rather than at a single one

In principle, our technique, including the data processing described below, allows the measurement of the reference signal only at one probe location outside of the medium of interest: for calibration purposes. The only reason why we have measured the reference signal for each location of the probe was that our current numerical implementation of the globally convergent algorithm works only with the case when the initializing wave field is a plane wave. On the other hand, a visual inspection of the output experimental data has revealed to us that actually we had a spherical rather than a plane wave. An extension of our numerical implementation to the case of the spherical wave is rather straightforward and we plan it for the future. We have used the point source rather than a plane wave in (1), (2) only to obtain the asymptotic behavior (16), which actually follows from the construction of the fundamental solution of the hyperbolic equation in [31, 32]. As it was mentioned in section 2, in computational practice we verify this asymptotic behavior numerically when working with plane waves, see subsection 7.2 of [3].

6   Data Processing

6.1   Data simulation

Since the computationally simulated data play an important role in our data processing procedure, we first describe the solution of the forward problem for equation (1). We have computationally simulated the solution of the forward problem for the reference medium. Since it is impossible to actually solve the PDE (1) in the entire space $\mathbb{R}^3$, we have solved it in a such a domain G that $\Omega \subset G$, where Ω is defined in (40). We took the domain $G = \{(x, y, z) \in [-3, 3] \times [-2, 2] \times [-5, 5]\}$. Our initializing plane wave was $v(t)$,

$$
v(t) = \begin{cases}
\sin(\omega t), & \text{for } t \in \left(0, \frac{2\pi}{\omega}\right), \\
0, & \text{for } t > \frac{2\pi}{\omega}, \\
\omega = 7.
\end{cases}
$$

Let ∂G_1 and ∂G_2 be respectively top and bottom sides of the prism G and $\partial G_3 = \partial G \setminus (\partial G_1 \cup \partial G_2)$ be the rest of the boundary of the domain G. We have numerically solved the following initial boundary value problem

$$
\begin{aligned}
\varepsilon_r(x)\, u_{tt} &= \triangle u, \quad \text{in } G \times (0, T), T = 12, \\
u(x, 0) &= 0, \ u_t(x, 0) = 0, \ \text{in } G, \\
\partial_n u\big|_{\partial G_1} &= v(t), \ \text{on } \partial G_1 \times (0, \frac{2\pi}{7}], \\
\partial_n u\big|_{\partial G_1} &= -\partial_t u, \ \text{on } \partial G_1 \times (t_1, T), \\
\partial_n u\big|_{\partial G_2} &= -\partial_t u, \ \text{on } \partial G_2 \times (0, T), \\
\partial_n u\big|_{\partial G_3} &= 0, \ \text{on } \partial G_3 \times (0, T),
\end{aligned}
\tag{43}
$$

In the case of data simulation for the reference medium we have in (43) $\varepsilon_r(x) \equiv 1$. We denote this solution as $u_{ref}(x, t)$. Thus, in (43) the plane wave is initialized at the top boundary ∂G_1 for $t \in (0, 2\pi/7)$ and propagates into G. First order absorbing boundary conditions [15] were used on the top boundary for $t \in (2\pi/7, T)$ and on the bottom boundary ∂G_2 for $t \in (0, T)$. The zero Neumann boundary condition is used on the rest of the boundary of the prism G. The latter boundary condition is used because the "pure" plane wave with $\varepsilon_r(x) \equiv 1$ satisfies this condition. The problem (43) was solved by the hybrid FEM/FDM method described in [7]. In this method, FDM is used outside of the domain Ω and FEM is used inside of this domain. The step size in the overlapping region was $\widetilde{h} = 0.2$, i.e. this was the same step size as the distance between neighboring probes.

6.2   Measured time resolved data

Denote $x_m \in P$ the location of the probe number m at the bottom side P of the prism Ω, see (41) for P. Figures 3-a)-d) display samples of curves and the label for Figure 3 explains details. The first arrival signal is when the burst starts. The signal before it is a
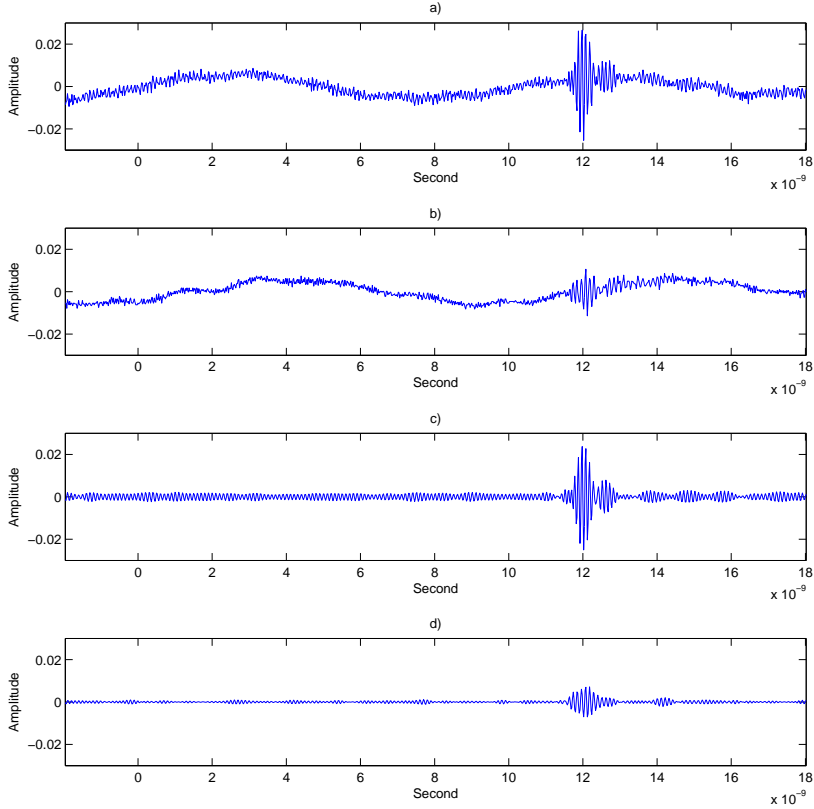
Figure 3. *a) A sample of the measured reference time resolved signal (i.e., no inclusion present) at the location $x_m \in P$ of the probe number m. b) The measured signal with inclusion present at the same probe location. The first burst starts when the EM wave arrives at the probe. The signal before this burst reflects a process within the probe itself. c) and d) represent signals a) and b) respectively after cleaning some noise via applying the Fast Fourier Transform procedure of MATLAB and truncating too low and too high frequencies. We are interested in the area of the first burst only. One can observe that the amplitude of the signal with the dielectric inclusion present (Fig. 3d) is generally less than one of the reference signal.*

low frequency signal reflecting some processes in the probe itself. It is obvious that the first thing to do is to perform the Fourier transform and truncate too low and too high frequencies. Low frequencies should be truncated to diminish the signal resulting from the probe itself. And high frequencies should be truncated to somehow decrease the noise further. We are interested in the first burst only. We see on Figs. 3-c),d) that the signal before this burst looks like a statistical noise. Even if it is not exactly a statistical noise, we have decided to subtract it from the data in the time interval where the first burst is. Let t_0 be the approximate time when the first burst starts and t_1 be the approximate time when this burst ends. Consider an interval (a, b) with $0 < a < b < t_0$ such that $b - a = t_1 - t_0$. For either of Figures 3-c) or 3-d) let $f_{a,b}(t)$ be the signal on this interval, and let the first burst be described by the function $\widetilde{f}(t), t \in (t_0, t_1)$. We have replaced $\widetilde{f}(t)$ with the function $f(t) = \widetilde{f}(t) - f_{a,b}(t - t_0 + a)$ for $t \in (t_0, t_1)$ and have worked with this function only after

20

this. Figure 4 displays of resulting superimposed curves for both reference signal and the signal with inclusion present. These curves are generated by Figures 3-c), d). We have also set to zero those parts of these curves which were before the first burst.
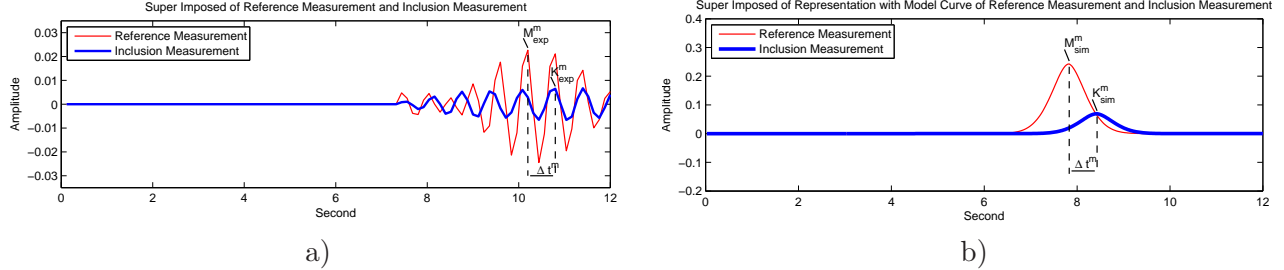
6.3 Immersing in the computationally simulated data

Figure 4. *This figure explains the idea of the immersing procedure in the time domain. a) Resulting superimposed experimental curves obtained from curves on Figures 3-a), b). The red curve is for the reference signal and the blue curve is for the signal with a dielectric inclusion present, both at the same location $x_m \in P$ of the probe number m. b) The red curve displays computationally simulated data $u_{ref}(x_m, t)$, also see sub-subsection 6.3.2. The blue curve $u_{incl}(x_m, t) = u_{ref}(x_m, t - \Delta t^m) K_{\exp}^m / M_{\exp}^m$ represents a sample of the immersed experimental data in the time domain at the same probe location $x_m \in P$, see explanations in sub-subsection 6.4.1. It is only the blue curve with which we work further. The red curve is displayed for the illustration purpose only.*

Consider now Figure 4-a) for a probe $x_m \in P$ number m. We have decided to "immerse" our experimental data in the computationally simulated data using the largest peak in the red curve (reference medium) with the peak value $M_{\exp}^m$ and the next peak after it in the blue curve (the medium with a dielectric inclusion present) with the peak value $K_{\exp}^m$. This next peak was chosen because the presence of a dielectric inclusion results in a time delay of the EM wave. This idea led us to a radically new data processing procedure described in this subsection. The immersing procedure in the computationally simulated data consists of two stages: immersing in the time domain and subsequent immersing in the pseudo frequency domain. We describe both of them sequentially. Below we talk about the computational simulated data in several places. In all cases these simulated data were computed *before* the experimental data were measured.

6.3.1 Stage 1. Immersing in time domain

Recall that the function $u_{ref}(x, t)$ is the solution of the problem (43) with computationally simulated data for $\varepsilon_r \equiv 1$. Obviously $u_{ref}\left(x^{(1)}, t\right) = u_{ref}\left(x^{(2)}, t\right), \forall x^{(1)}, x^{(2)} \in P, \forall t \in (0, T)$. Let $t := t_{ref}^{sim}$ be such a moment of time that for all $x \in P$ we have $u_{ref}(x, t) = 0$ for $t < t_{ref}^{sim}$ and $u_{ref}(x, t) > 0$ for such moments of time t that are rather close to t_{ref}^{sim} with $t > t_{ref}^{sim}$, see the reference curve (red) on Figure 4-b). Naturally, we call t_{ref}^{sim} the *time of the first arrival of the computationally simulated EM wave field* $u(x, t) = u_{ref}(x, t)$ in (43) at the plane P.

21

Important Observation and Conclusion. We have observed in our computational simulations that for those values of $t > t_{ref}^{sim}$, which are rather close to t_{ref}^{sim}, the only side of Ω which is sensitive to the presence of a dielectric inclusion, is the bottom side P of the domain Ω. Other five sides of the prism Ω are not sensitive to the presence of inclusions for those values of t. In other words, the values of the function u at those sides are approximately the same ones as those for the reference medium. This important observation led us to the conclusion that we should work only with the information contained in the first burst, see Figure 4-a). Actually, this idea corresponds well with the common knowledge of physics that the most informative signal is the one which is collected at those times t, which are close to the moment of the first arrival of the signal.

The next important question was: *How to work with this first burst?* Indeed, we have observed on experimental curves that the amplitude of the signal near the time of the first arrival at a probe is so weak that it this signal cannot be differentiated from the noise, see Figure 4-a). Consider the reference experimental signal at the probe $x_m \in P$, see Figure 4-a). We have decided that we should work with the largest upwards looking peak. If, however we have several peak values with no more than 10% difference between them, then we choose the earliest among those, i.e. we choose such a peak which corresponds to the minimal value of t. We have done this as follows. Let $y_m = y_m(t)$ be the experimentally measured function at the point x_m (after the above noise reduction). Suppose that on the first burst we have local maxima at points $\{t_1, ..., t_n\}$ and their values are $\widetilde{y}_1 = y_m(t_1), .., \widetilde{y}_n = y_m(t_n)$. Let $Y = y_m(t_k) = \max_{i=1,...,n} y_m(t_i)$. Consider numbers $\widetilde{y}^1 = y(t^1), ..., \widetilde{y}^r = \widetilde{y}(t^r)$, where points $\{t^1, ..., t^r\} \subset \{t_1, ..., t_n\}$ are such that $\widetilde{y}^j / Y \in [0.9, 1]$. And let $t^m = \min\{t^1, ..., t^r\}$. We choose the pair $(t^m, \widetilde{y}^m)$ and denote $(t^m, \widetilde{y}^m) := \left(t_{ref}^{\exp}(m), M_{\exp}^m\right)$.

Next, we choose a local maximum for the experimental curve at $\{x_m\}$ for the medium with a dielectric inclusion present. Let $z_m = z_m(t)$ be that curve (after the above noise reduction). Consider local maxima of this function for $t \geq t_{ref}^{\exp}(m)$. Let $t_{incl}^{\exp}(m) \geq t_{ref}^{\exp}(m)$ be the minimal value of the time t on the interval $\left\{t \geq t_{ref}^{\exp}(m)\right\}$ at which a local maximum of the function $z_m(t)$ is achieved. In other words, we choose the first upwards looking peak of the function $z_m(t)$ occurring after the prior chosen reference peak at the reference curve. Denote $z_m\left(t_{ref}^{\exp}(m)\right) := K_{\exp}^m$. So, $K_{\exp}^m$ is the value of that peak, see Figure 4-a). However, if $K_{\exp}^m / M_{\exp}^m \geq 2/3$, then we set for the point $\{x_m\}$ that $\left(t_{incl}^{\exp}(m), K_{\exp}^m\right) := \left(t_{ref}^{\exp}(m), M_{\exp}^m\right)$. We have observed that on all probes $K_{\exp}^m \leq M_{\exp}^m$.

Now we are ready to immerse our data in the computationally simulated data. Let $u(x, t)$ be the solution of the problem (43) with $\varepsilon_r(x) \equiv 1$, i.e. the function $u(x, t)$ describes the plane wave propagation in the uniform medium. Let $x_m \in P$ be the location of the probe number m. Let $\Delta t^m = t_{incl}^{\exp}(m) - t_{ref}^{\exp}(m)$ be the time shift between two above chosen peaks for this probe, see Figure 4-a). Then we set

$$u_{incl}(x_m, t) = \frac{K_{\exp}^m}{M_{\exp}^m} u_{ref}(x_m, t - \Delta t^m). \tag{44}$$

So, (44) is our *immersed data in the time domain* for the probe number m. Figure 4-b) illustrates (44). It is clear from the above that if $K_{\exp}^m / M_{\exp}^m \geq 2/3$, then $u_{incl}(x_m, t) =$

$u_{ref}(x_m, t)$. Below we work only with so immersed data for each probe location on the surface P. We work further with these immersed data to ultimately use them as an input for the Dirichlet boundary conditions $\psi_n(x), x \in P$ in equations (17). Thus, since we actually use ratios $K_{\exp}^m / M_{\exp}^m$, we do not need to know the value A of the signal's amplitude in (39).

6.3.2 Stage 2. Immersing in the pseudo frequency domain

We should apply the Laplace transform (7) to each curve $u_{incl}(x_m, t)$ in (44) to obtain the function $w_{incl}(x_m, s) = \mathcal{L}(u_{incl}(x_m, t))$. The next question is: *For what values of the pseudo frequency s should we actually calculate the integral (7)?* To address this question, we have solved the above CIP for the domain Ω in (40) for a computationally simulated data with an inclusion present, using the above globally convergent numerical method. This was done prior obtaining the experimental data. We have established that the following numbers are optimal ones

$$s \in [3.5, 7.5], h = 0.5. \tag{45}$$

So, we have calculated the numbers $w_{incl}(x_m, s)$ for nine values of s in (45) for each probe location $x_m \in P$. Below in this sub-subsection we work only with values of s from (45). We have observed computationally that, because of the rapid decay of the function $\exp(-st)$ with respect to t for values of s from (45), the major impact in the integral (7) comes from the first splash of the curve $u_{ref}(x_m, t)$. So, only this splash is depicted on Figure 4-b).

Let $\widetilde{w}_{incl}(x_m, s) = -(\ln w_{incl}(x_m, s))/s^2$ and for each value s from (45) let $\widetilde{w}_{incl}(x, s)$ be the linear interpolation of discrete values $\{\widetilde{w}_{incl}(x_m, s)\}$ over P. The function $\widetilde{w}_{incl}(x, s)$ is very noisy with respect to $x \in P$, e.g. see Figure 5-a). On the other hand, Figure 5-b) displays a typical $x-$ dependence of the function $\widetilde{w}_{sim}(x, \overline{s}) := -(\ln w_{sim}(x, \overline{s}))/\overline{s}^2, x \in P$, where the function $w_{sim}(x, s)$ is corresponds to a sample of computationally simulated data for an inclusion present. Again, this data simulation took place prior the experimental data were obtained. Hence, to make our resulting function look like the one on Figure 5-b), we have smoothed the function $\widetilde{w}_{incl}(x, s)$ over $x \in P$ via the so-called Lowess Fitting in the 2-D case, which we took from MATLABR 2009a. A sample of the resulting function $\widetilde{w}_{smooth}(x, \overline{s})$ for $s := \overline{s}$ is displayed on Figure 5-c). Still, however, this function does not yet look similar to the function depicted on Figure 5-c). Define the number $W_{ref}(s)$ as follows (see (7)) $W_{ref}(s) = -s^{-2} \ln \mathcal{L}(u_{ref})$, for $x \in P$. We took

$$\widetilde{w}_{immers}(x, s) = \begin{cases} \widetilde{w}_{smooth}(x, s), & \text{if } \widetilde{w}_{smooth}(x, s) \geq 0.985 \max_{\overline{P}}(\widetilde{w}_{smooth}(x, s)), \\ W_{ref}, & \text{otherwise,} \end{cases}$$

see Figure 5-d), which depicts the function $\widetilde{w}_{immers}(x, \overline{s})$. We call the function $\widetilde{w}_{immers}(x, s)$ the *immersed data in the pseudo frequency domain*. Thus, we work with the function $\widetilde{w}_{immers}(x, s)$ to obtain functions $\psi_n(x), x \in P$ in (17). Namely, we use finite differences to approximately compute the s-derivative. Recalling that $\widetilde{w}(x, s) := -(\ln w(x, s))/s^2$, we obtain for the finite difference

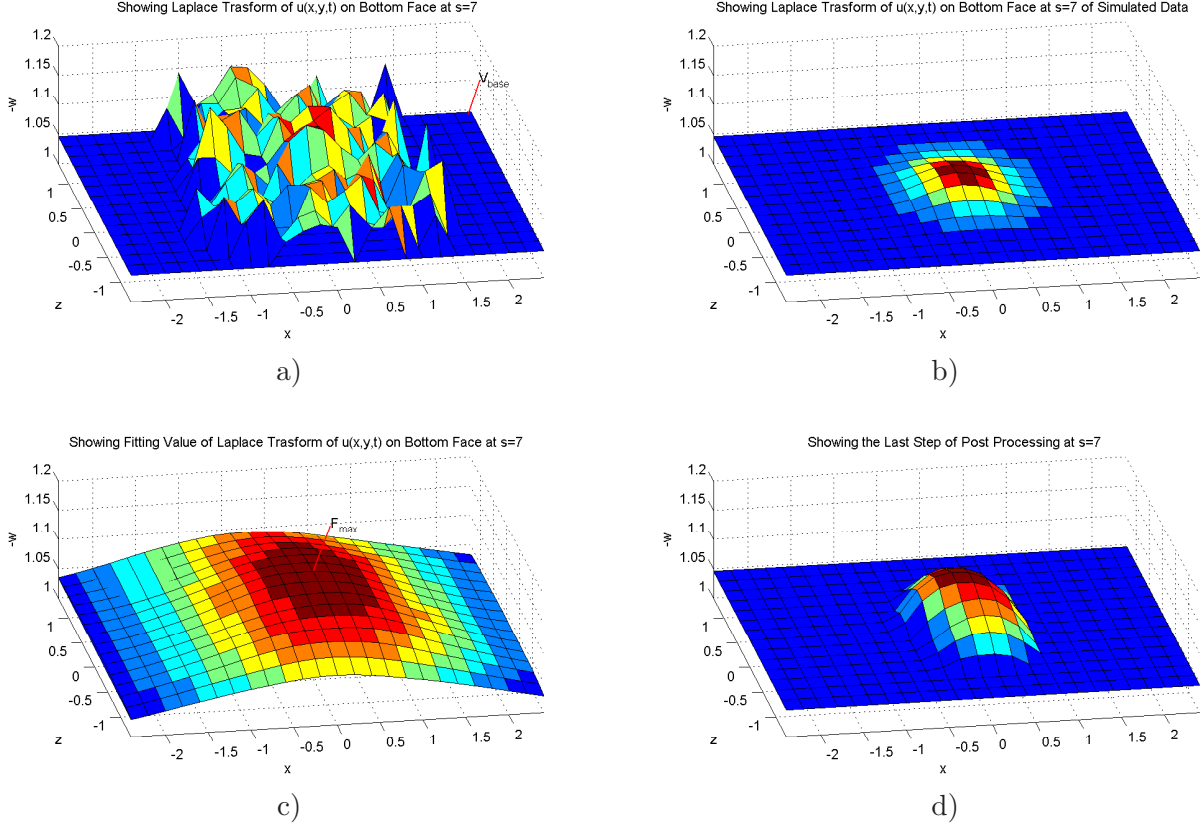$$\psi_n(x) = \frac{\widetilde{w}_{immers}(x, s_n - 0.5) - \widetilde{w}_{immers}(x, s_n)}{0.5}, x \in P. \tag{46}$$

Figure 5. *a) The function $\widetilde{w}_{incl}(x,\overline{s})$, $\overline{s} = 7.5$. b) The function $-(\ln w_{sim}(x,\overline{s}))/\overline{s}^2$ is depicted, where $w_{sim}(x,\overline{s})$ is the Laplace transform (7) of the function $u_{sim}(x,t)$ for a computationally simulated data. Figure 5-b) is given only for the sake of comparison with Figure 5-a). c) The function $\widetilde{w}_{smooth}(x,\overline{s})$ resulting from fitting of a) by the Lowess Fitting procedure in the 2-D case, see MATLABR 2009a. d) The final function $\widetilde{w}_{immers}(x,\overline{s})$. Values of $\widetilde{w}_{immers}(x,s)$ are used to produce the Dirichlet boundary conditions $\psi_n(x)$ for PDEs (17) of the globally convergent algorithm, see (47).*

As to the values of the function $\psi_n(x)$ on other five sides of the prism Ω, they were computed by the same finite difference formula using the function resulting from the function $\mathcal{L}(u_{ref})$.

6.3.3   Physics considerations for data immersing

The above immersing procedure in the time domain makes sense from the physics standpoint. Since our assumption is that the relative permittivity in the domain of interest Ω is $\varepsilon_r \geq 1$, then by (3) the EM wave should propagate through Ω slower than through the air. In other words, the so-called time delay should take place, and this is why (44) makes sense. Still, it is unclear how to actually quantify the previous statement. Furthermore, we doubt that it is known *what exactly* that statement means in terms of the experimental data. Does it relate to the truly first arrival signal, which is too weak to be trusted? Or perhaps it is related to the largest peak values as we have chosen? Or maybe this is related to the first burst "as a

whole"?

However, if we assume that the first largest peak value (although within 90% tolerance level) for the reference medium arrives earlier for the air than the one for the case of a heterogeneous medium, then the above choice of peak values makes sense. It seems to be that our results (subsection 8.4) justify the latter assumption. Also, using only one point $(t^m, \widetilde{y}^m)$ for the reference signal and only one point $(t^m_{incl}, z_m(t^m_{incl}))$ of the signal with an inclusion present does not mean of course that we have actually used only this single point. Indeed, to figure out which exactly point should be chosen, we have counted all local maxima in the first burst and thus, have examined the entire curve.

7 Some Details of the Numerical Implementation of the Globally Convergent Algorithm

We point out that all details of the numerical implementation of the globally convergent algorithm, which are described in this section, were implemented *prior* obtaining the experimental data. The same is related to all results for computationally simulated data mentioned in the above sections. When working with the experimental data, we have not changed our original numerical code for the inverse problem solution and thus have not changed features listed in the next subsection. In other words, our computations of images from experimental data were unbiased. We have implemented all these details listed in subsection 7.1 when working with those computationally simulated data. When implementing these details, our goal was twofold: **(1)** to obtain the best performance of the globally convergent algorithm, and **(2)** at the same time, still to remain "within" conditions of Theorem 1.

7.1 Details

All details listed in this subsection were implemented when we were working with computationally simulated data, which was prior obtaining experimental data. We have observed in our computational simulations that values of $|V_{n,k}(x, \overline{s})|$ of approximations for the tail function dominate values of all other terms in equations (17) for functions $q_{n,k}$. Hence, when solving equations (17) for functions $q_{n,i}$ (subsection 3.1) in our computations, we have used in (17) $\overline{s}$-derivatives of tails $\partial_{\overline{s}} V_{n,i}(x, \overline{s})$ instead of tails $V_{n,i}(x, \overline{s})$ themselves. These derivatives were taken via finite differences, similarly with (47). However, when computing functions $\varepsilon_r^{(n,i)}(x)$ via (18a,b), we have still used in (18b) the function $V_{n,i}(x, \overline{s})$ itself. The parameter in the Carleman Weight Function was $\mu = 50$. Likewise, we have made cut-offs of computed functions $\varepsilon_r^{(n,i)}(x)$ as follows. For each n we have chosen a cut-off value $C_{cut}(n)$ such that we have assigned a new value $\widetilde{\varepsilon}_r^{(n,i)}(x)$ for the function $\varepsilon_r^{(n,i)}(x)$ as

$$\widetilde{\varepsilon}_r^{(n,i)}(x) = \begin{cases} \varepsilon_r^{(n,i)}(x), & \text{if } \varepsilon_r^{(n,i)}(x) > 1 + C_{cut}(n), \\ 1, & \text{if } \varepsilon_r^{(n,i)}(x) \in [1, 1 + C_{cut}(n)]. \end{cases} \tag{47}$$

Note that by (18a) $\varepsilon_r^{(n,i)}(x) \geq 1$, $\forall x \in \Omega$. The numbers C_{cut} were chosen as follows

$$C_{cut}(1) = 0, C_{cut}(2) = 0.2, C_{cut}(3) = C_{cut}(4) = 0.8, C_{cut}(5) = 0.6,$$
$$C_{cut}(6) = C_{cut}(7) = 0.4, C_{cut}(8) = 0.8.$$

We now define stopping rules of iterations for functions $q_{n,1}^k$ with respect to the nonlinear term as well as for functions $\{q_{n,k}\}$ with respect to the tails. These rules are almost the same as ones in [4]. Consider the planar surface $P_{\widetilde{h}}$ which is parallel to the surface P in (41). The surface $P_{\widetilde{h}}$ is obtained from the surface P via shifting upwards by $\widetilde{h} = 0.2$,

$$P_{\widetilde{h}} = \left\{(x, y, z) : (x, y) \in [-2.4, 2.4] \times [-1.4, -1.4], z = -2.4 + \widetilde{h} = -2.2\right\}.$$

And let $\Omega' = \{(x, y) \in [-2.4, 2.4] \times [-1.4, -1.4]\}$ be the orthogonal projection of both surfaces P and $P_{\widetilde{h}}$ on the (x, y) plane. Consider norms $F_n^k = ||q_{n,1}^k|_{P_{\widetilde{h}}} - \overline{\psi}_n||_{L_2(\Omega')}$. We stop iterations of functions $q_{n,1}^k$ when either $F_n^{k+1} \geq F_n^k$, or norms F_n^k stabilize, or $F_n^k \leq \varepsilon$, where $\varepsilon = 0.001$ is a small tolerance number of our choice. Next, we iterate with respect to the tails. We similarly introduce norms $F_{n,i} = ||q_{n,i}|_{P_{\widetilde{h}}} - \overline{\psi}_n||_{L_2(\Omega')}$ and use the same stopping rule as one for F_n^k.

While stopping rules for iterations of functions $q_{n,1}^k$ and $q_{n,i}$ was the same as one in [4], the stopping rule for computing functions $\varepsilon_r^{(n)}(x)$ is now different from [4]. Namely, let

$$a_n = \frac{\left\|\varepsilon_r^{(n)} - \varepsilon_r^{(n-1)}\right\|_{L_2(\Omega)}}{\left\|\varepsilon_r^{(n-1)}\right\|_{L_2(\Omega)}}, \quad b_n = \frac{a_n}{a_{n-1}}.$$

Stopping rule for $\varepsilon_r^{(n)}$:

$$\text{If} \begin{cases} b_n \in [1.9, 4] \text{ and } n > 3, \text{ then take the final solution } \varepsilon_r^f = \varepsilon_r^{(n)}, \\ b_n > 4 \text{ and } n > 3, \text{ then take the final solution } \varepsilon_r^f = \varepsilon_r^{(n-1)}, \\ \qquad \text{alternatively compute } \varepsilon_r^{(n+1)}. \end{cases} \quad (48)$$

We have chosen $n > 3$ in (48) because we have observed in our work with computationally simulated data that images are becoming more or less close to the correct ones only starting from $n = 4$. And this is in a conjunction with the convergence estimate (33).

7.2   Analytical aspects of details of the numerical implementation

Consider the analytical aspect of details listed in subsection 7.1. Note that the exact meaning of words "large" and "small" (in terms of used numbers) depends on a specific numerical implementation, and so, from this standpoint, we can assume that the s-interval (45) corresponds to large values of s and the interval (45) is small. It follows from (16) that one should expect that

$$|\partial_{\overline{s}} V(x, \overline{s})|_{2+\alpha} << |V(x, \overline{s})|_{2+\alpha}. \quad (49)$$

Denote $\widetilde{V}_{n,i}(x,\overline{s}) = \partial_{\overline{s}} V_{n,i}(x,\overline{s})$. It follows from (49) that for large $\overline{s}$ we have an analog of the right inequality (28), $\left|\widetilde{V}_{n,i}(x,\overline{s})\right|_{2+\alpha} \leq \xi$ for a small parameter ξ, whereas the left inequality (28) is still valid. It easily follows from the proof of the global convergence theorem in [4] that Theorem 1 is still valid when tails $V_{n,i}(x,\overline{s})$ are replaced with $\widetilde{V}_{n,i}(x,\overline{s})$. Therefore, the replacement of $V_{n,i}(x,\overline{s})$ with $\partial_{\overline{s}} V_{n,i}(x,\overline{s})$ corresponds well with the above new mathematical model (sub-subsection 3.3.2). This is because by this model one considers the number ξ, which bounds norms of tails from the above, as a parameter, which can be made infinitely small independently on the value of $\overline{s}$. So, we conclude that in our computations we have indeed used the above new mathematical model. As to the cut-offs (47), such cut-offs are routinely used in imaging as post processing procedures.

8   Imaging Results

8.1   Abnormalities and their positions

Our abnormalities to be imaged were two wooden cubes, see Table 1.

Table 1. *Sizes of two wooden cubes*

Cube number	Original sizes, mm	Dimensionless sizes
1	$40 \times 40 \times 40$	$0.8 \times 0.8 \times 0.8$
2	$60 \times 60 \times 60$	$1.2 \times 1.2 \times 1.2$

Let CL be the center line, i.e. the straight line which is orthogonal to the plane P and which passes through the source of EM waves (Figure 1). Then $CL = \{(x,y,z) : x = y = 0\}$. We have placed both those cubes in two positions. In the first position the center of the cube was on CL. In the second position the center of the cube was shifted off CL by 10 mm in the positive direction of x-axis (0.2 in dimensionless units). In addition, we have used the third position for the cube number 1. This position was quite off CL. Namely, in the third position the center of this cube was shifted off CL by 60 mm in the positive direction of the x-axis (1.2 in dimensionless variables). We have observed on the experimental data that since we had a spherical rather than a plane wave, the magnitude of the EM field has decayed quite significantly when the point has moved rather far off CL. So, the goal of placing the cube number 1 in the third position was to see how this decay of the magnitude of the EM field would affect the image quality. Because of some logistical reasons, we did not put cube number 2 in this third position. Likewise, because of logistical reasons, we have measured the scattering field from cube number 1 in the first position twice: in two consecutive days. Therefore, we have obtained total six (6) pieces of data for the case of an inclusion present. In addition, the data for the reference medium, was measured only once. Table 2 lists all six cases.

Table 2. *Positions of centers of two wooden cubes to be imaged in six cases. The difference between cases 1.1(1) and 1.1(2) is that they were measured on two different days for the same position of cube 1*

Cube Number	Case Number	Center
1	1.1(1)	$(0, 0, -1.2)$
1	1.1(2)	$(0, 0, -1.2)$
1	1.2	$(0.2, 0, -1.2)$
1	1.3	$(1.2, 0, -1.2)$
2	2.1	$(0, 0, -1.2)$
2	2.2	$(0.2, 0, -1.2)$

8.2   Tables and images

We have made computations using the above described globally convergent algorithm and functions $\psi_n(x)$ in (46). We have used the stopping rules described in subsection 7.1. We point out again that we did not know in advance values refractive indexes of our wooden cubes. Therefore, when applying stopping rules, we were *unbiased*. Table 3 presents numbers a_n and $b_n = a_n/a_{n-1}$ for the case 1.1(1) (see Table 2 for labeling of our cases). Behavior of these numbers for other cases was similar. Therefore, Table 4 presents only numbers b_n^f for the final iteration. Figures 6 and 7 display computed images. Our goal was twofold: (1) to obtain accurate locations of inclusions and (2) to accurately image refractive indexes in them. However, we did not have a goal to accurately image shapes of inclusions.

Table 3. *Computational results for the case 1.1(1), see Table 2 for labeling of cases and (49) for the stopping rule*

Iter., n	$\varepsilon_r^{(n)}$	a_n	b_n	ε_r^f	$n_f = \sqrt{\varepsilon_r^f}$
2	1.28	0.027	0.21		
3	2.53	0.209	7.74		
4	2.9	0.160	0.76		
5	3.76	0.266	1.66		
6	4.66	0.580	2.18	$\varepsilon_r^f = \varepsilon_r^{(6)} = 4.66$	2.16
7	5.6	0.683	1.18		
8	8.1	0.809	1.18		

8.3   Accuracy of the blind quantifiable imaging

We have independently measured refractive indexes *after* the above images were obtained. Those measurements were performed by two well established methods: the Waveguide Method [30] and the Oscilloscope Method, see [17] and http://www.tek.com/learning/oscilloscopes for the latter method. Tables 5 and 6 display comparisons of our computational results with measured ones, along with both measurement and imaging errors. One can see the error in

Table 4. *Computational results for five cases, see (48) for the stopping rule and Table 2 for labeling of cases. The rest of iterations for all these five cases was similar with Table 3. Comparison of Table 4 with (48) makes it clear why either of function $\varepsilon_r^{(n)}$ or $\varepsilon_r^{(n-1)}$ was chosen as the final imaging result ε_r^f*

Case	Iter., n	b_n	ε_r^f	$n_f = \sqrt{\varepsilon_r^f}$
1.1(2)	5	2.07	$\varepsilon_r^f := \varepsilon_r^{(5)} = 4$	2
1.2	6	2.40	$\varepsilon_r^f := \varepsilon_r^{(6)} = 4.65$	2.16
1.3	6	3.57	$\varepsilon_r^f := \varepsilon_r^{(6)} = 4.82$	2.19
2.1	6	5.74	$\varepsilon_r^f := \varepsilon_r^{(5)} = 2.98$	1.73
2.2	6	5.36	$\varepsilon_r^f := \varepsilon_r^{(5)} = 3.19$	1.79

our computations did not exceed the measurement error in all cases except of the case 1.1(2) in Table 6, in which our error was 1.8% more than the measurement error.

Table 5. *Comparison of imaging results of values of refractive indexes for six cases of Table 2 with measurements by the Waveguide Method*
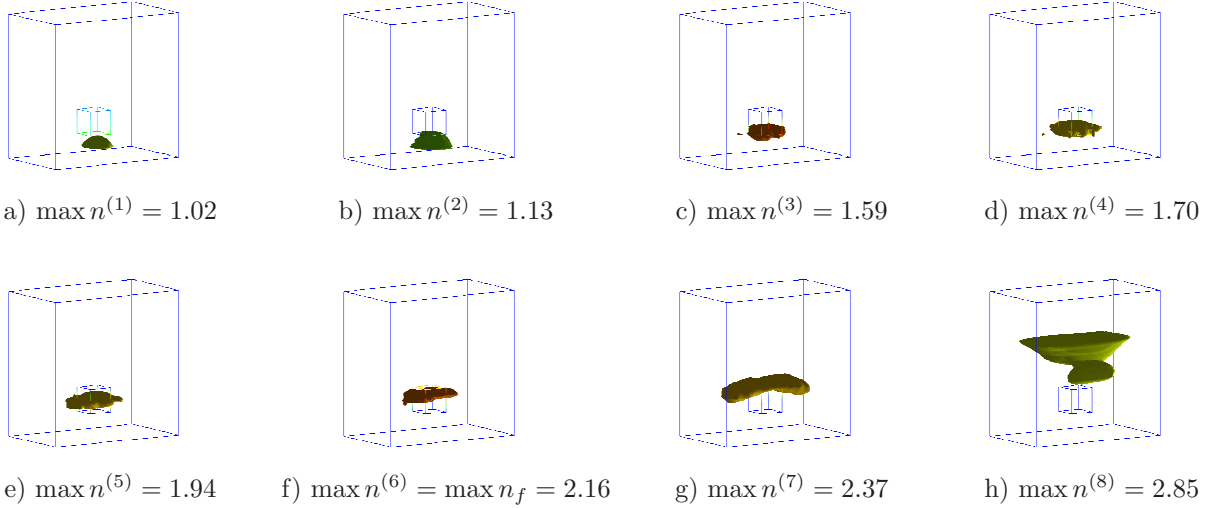
Case	Blindly imaged $n := n_f$	Measured n, error	Imaging error
1.1(1)	2.16	2.07, 11%	4.3%
1.1(2)	2	2.07, 11%	3.4%
1.2	2.16	2.07, 11%	4.3%
1.3	2.19	2.07, 11%	5.8%
2.1	1.73	1.71, 3.5%	1.2%
2.2	1.79	1.71, 3.5%	4.7%

Table 6. *Comparison of imaging results of values of refractive indexes for six cases of Table 2 with measurements by the Oscilloscope Method*

Case	Blindly imaged $n := n_f$	Measured n, error	Imaging error
1.1(1)	2.16	2.17, 6%	0.5%
1.1(2)	2	2.17, 6%	7.8%
1.2	2.16	2.17, 6%	0.5%
1.3	2.19	2.17, 6%	1%
2.1	1.73	1.78, 6%	2.8%
2.2	1.79	1.78, 6%	0.56%

8.4   Performance of the modified gradient method (38)

Temporary denote $\mathbf{x} = (x, y, z)$. We have also applied the modified gradient method (38) to the experimental data. Our starting point was $\varepsilon_r^{(0)} \equiv 1$. In other words, since any gradient-like method is a locally convergent one, we have assumed that we know the background medium in the domain Ω, unlike the globally convergent method. We have observed that

a) $\max n^{(1)} = 1.02$ b) $\max n^{(2)} = 1.13$ c) $\max n^{(3)} = 1.59$ d) $\max n^{(4)} = 1.70$

e) $\max n^{(5)} = 1.94$ f) $\max n^{(6)} = \max n_f = 2.16$ g) $\max n^{(7)} = 2.37$ h) $\max n^{(8)} = 2.85$

Figures 6-a)-h) *show the dynamics of the sequence of images for the case number 1.1(1). Maximal values of refractive indexes $\max_{\overline{P}} n^{(k)} = \sqrt{\max_{\overline{P}} \varepsilon_r^{(k)}}$ are displayed. Each image represents the level surface $\{x{:}n^{(k)}(x) = max_{\overline{P}}n^{(k)}(x)\}$. The final image is presented on f). h) shows that the image "explodes" on the second iteration after the stop, see the Stopping rule (48) and Table 3.*
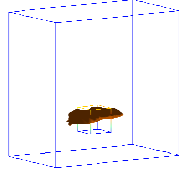
the function $\lambda\left(\mathbf{x}, s, \varepsilon_r^{(0)}\right) = \lambda\left(\mathbf{x}, s, 1\right) < 0$. At the same time, we saw that the function $w\left(\mathbf{x}, s, 1\right) > 0$. Hence, it follows from (38) that $\varepsilon_r^{(1)} < 1$, where $\varepsilon_r^{(1)}$ is the result of the first iteration of the solution of the problem (38) with the contraction mapping operator. We have tried a variety of numbers c_1, c_2, θ in (38), some of which have ensured the contraction mapping property. Still, in all iterations and with all these parameters we have obtained functions $\varepsilon_r^{(n)} < 1$ for all iteration numbers n, which contradicts with (4).

We have an almost rigorous explanation for the negative values of the function $\lambda\left(\mathbf{x}, s, 1\right)$. It is clear from Figure 5-d) that we can approximately assume that the domain Ω is the half space$\{z > -2.4\}$ (see (40)). Changing variables $z' := z + 2.4$ and leaving the same notation for the new variable as one for the old one (for brevity), we obtain $\Omega = \{z > 0\}$. In addition, assume that the condition $\lim_{|x| \to \infty} \lambda\left(\mathbf{x}, s, 1\right) = 0$ is imposed and also that $\lim_{|\mathbf{x}| \to \infty} \left(w \mid_{z=0} -\widetilde{g}\right) = 0$. Consider the function $Q\left(\mathbf{x}, \boldsymbol{\xi}\right)$,

$$Q\left(\mathbf{x}, \boldsymbol{\xi}\right) = \frac{\exp\left(-s\left|\mathbf{x} - \boldsymbol{\xi}\right|\right)}{4\pi\left|\mathbf{x} - \boldsymbol{\xi}\right|} + \frac{\exp\left(-s\left|\mathbf{x} - \boldsymbol{\xi}'\right|\right)}{4\pi\left|\mathbf{x} - \boldsymbol{\xi}'\right|}, \boldsymbol{\xi}' = \left(\xi_1, \xi_2, -\xi_3\right).$$

It can be easily verified that $Q\left(\mathbf{x}, \boldsymbol{\xi}\right)$ is the Green's function with the Neumann boundary condition in the half space $\{z > 0\}$ for the operator $\Delta - s^2$. Hence, by (35)
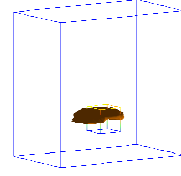
$$\lambda\left(\mathbf{x}, s, 1\right) = \int_{\mathbb{R}^2} Q\left(\mathbf{x}, \xi_1, \xi_2, 0\right)\left[w\left(\left(\xi_1, \xi_2, 0\right), s, 1\right) - \widetilde{g}\left(\xi_1, \xi_2, s\right)\right] d\xi_1 d\xi_2.$$
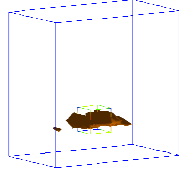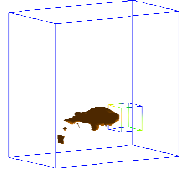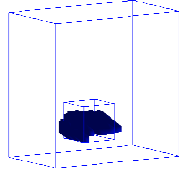
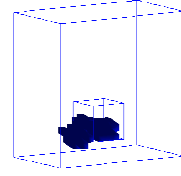a) Case 1.1(1), $\max n_f = 2.16$ b) Case 1.1(2), $\max n_f = 2$ c) Case 1.2, $\max n_f = 2.16$

d) Case 1.3, $\max n_f = 2.19$ e) Case 2.1, $\max n_f = 1.73$ f) Case 2.2, $\max n_f = 1.79$

Figures 7-a)-f) display resulting images. It should be kept in mind that we did not have a goal to image shapes of inclusions accurately. Rather, our goal was only to image their locations and maximal values of refractive indexes $n_f(x) = \sqrt{\varepsilon_r^f}$. On each figure $n_f(x) = \max n_f$ for all points of the image of the corresponding cube. In addition to the cut-offs (47), we have made the last post processing cut-off of the imaged function ε_r^f on each figure just to make it look better. That cut-off was made around the center of the image. For all cases the dynamics of the change of images of functions $\varepsilon_r^{(n)}$ with iterations was similar with one on Figures 6-a)-h).

The function $w\left((\xi_1, \xi_2, 0), s, 1\right)$ is obtained via solving the boundary value problem (35) at $\varepsilon_r := 1$. We have observed computationally that $w\left((\xi_1, \xi_2, 0), s, 1\right) - \widetilde{g}\left(\xi_1, \xi_2, s\right) \leq 0, \forall (\xi_1, \xi_2) \in \mathbb{R}^2$ and $meas \left\{w\left(\xi_1, \xi_2, 0\right), s, 1 - \widetilde{g}\left(\xi_1, \xi_2, s\right)\right\} < 0) > 0$ for all reasonable values of s. Hence, $\lambda(\mathbf{x}, s, 1) \leq 0$.

In addition, we have observed computationally that for all reasonable values of the pseudo frequency s maximal absolute values of functions w and λ were too small. So that $\max_{\overline{\Omega}} s^2 |w\lambda| \leq 3 \cdot 10^{-4}$. By (38) this means, however, that in order for the function ε_r to be rather significantly different from $\varepsilon_r^{(0)} \equiv 1$, i.e. in order to obtain above inclusion/background contrasts, one should choose a very small regularization parameter θ. For example, to get $\varepsilon_r^f = 4.66$ within the imaged inclusion (Table 3), one should have $\theta \approx 8 \cdot 10^{-5}$. It is well known, however, that exceedingly small values of regularization parameters affect results quite negatively: those parameters should be actually larger than the level of error both in the mathematical model and in the data.

We, therefore conclude that the modified gradient method (38) is inapplicable here. However, since any version of the gradient method should still use the gradient $E'(\varepsilon_r)$, which is derived in section 4, then it is unlikely that other versions of the gradient method are applicable here. This likely means that locally convergent numerical methods are inapplicable in the pseudo frequency domain. Thus, it seems to be at this moment that our globally convergent technique is the *single* choice for this kind of experimental data.

9 Discussion

The goal of this research effort was to verify the globally convergent numerical method of [3, 4, 5, 6] experimentally. We have arranged picosecond scale time resolved measurements to acquire the data scattered by small dielectric abnormalities ($1ps = 10^{-12} \sec = 10^{-3} ns$). The time resolved data were measured in the tomographic manner on a planar surface, which was opposite to the single source location used. This constitutes to a *minimal* amount of information gathered, which is important for such applications as, e.g. imaging of land mines, imaging of baggages in airports, more generally, imaging of explosives and also imaging of defects in non-distractive testing. Furthermore, the technique of [3, 4, 5, 6] can be extended to the most practically interesting case of stand off detection using the back reflected data only [23].

At each location of the detector the data were collected for total of 12,300 picoseconds, i.e. 12.3 nanoseconds. A radically new data processing procedure was developed. The goal of this procedure was to adapt the data to the mathematical model, which is based on the hyperbolic equation (1). Results of the data processing were used as in input for the globally convergent numerical method of [3, 4, 5, 6] for the CIP (1), (2), (6). While processing the data, we have used the fact that on five out of six sides of the prism Ω the data were not sensitive to the presence of inclusions and thus we have assigned values taken from the reference medium for them. The only sensitive side was the planar surface P of our measurements. However, as soon as the data are pre-processed, our algorithm does not use any a priori knowledge neither about the background values of the unknown coefficient, nor about locations of inclusions. The only information it uses is that the value of the refractive index outside of the computational domain of interest is the same as one in the air and that the refractive index in the computational domain is not less than the one in the air. Our algorithm solves a fully nonlinear problem. No linearization is used. Our computations were quite fast and took only a few minutes on a regular PC to get the above images. This points towards a possibility to obtain real time imaging after a certain programming effort.

We have formulated the global convergence theorem of [4] for our method and have discussed its features in detail. This theorem has a problem with the truncation of the pseudo frequency $\overline{s}$, since we cannot prove convergence as $\overline{s} \to \infty$. Furthermore, if we would somehow prove this convergence, then we would address a long standing and well known question about uniqueness theorem for the Coefficient Inverse Problem (1), (2), (6). In addition, we have pointed out that a similar issue exists in the classic Real Analysis in connection with asymptotic series expansions of some functions, although still those expansions are known to provide good approximations. We have also pointed out to a similar problem with the truncation of the Fourier series in the Gelfand-Krein-Levitan reconstruction method for a 2-D hyperbolic CIP, although numerical results demonstrate an excellent performance of this method [20].

Thus, we have concluded that the only way to justify such truncations is via numerical studies. This was done successfully in [3, 4, 5, 6] for computationally simulated data and also for the experimental data in the current paper. We believe that the success in these numerical

studies has the same nature as routine truncations of high frequencies in engineering. Indeed, it is well known that in engineering high frequencies are often truncated without any proofs of convergence and things still work well.

Since the question about convergence at $\overline{s} \to \infty$ is very challenging to address, we have proposed a new mathematical model for our numerical method. We believe that this model intrinsically has the same nature as the above mentioned truncation of asymptotic series. By our model, a certain small positive parameter ξ is allowed to be infinitely small independently on the truncation pseudo frequency $\overline{s}$, although formally it does depend on $\overline{s}$. Furthermore, it turns out that we have benefited from this model via applying it in computations (subsection 7.1). It is also important to point out that all features of our numerical implementation mentioned in subsection 7.1 were pre-arranged prior getting experimental data. Therefore, we were not biased when computing above results. Our stopping criterion, which truncates iterations, is in a full agreement with one of backbone ideas of the theory of Ill-Posed Problems, see pages 156 and 157 in [14]. By this idea, the iteration number can be used as a regularization parameter.

In fact, we had semi blind testing. In other words, we knew locations of inclusions, although this information is not used in our algorithm. However, we were unaware about values of refractive indexes in them. So, with respect to the values of the refractive indexes we were *blind*. We have verified a posteriori results of our computations via direct measurements using two well established methods of Physics. These measurements have revealed that our computational results for experimental data have consistently demonstrated an excellent accuracy in six (6) out of six (6) cases, i.e. in 100% available cases. In all cases, our computational error was either less or no more than 1.8% that the measurement error. An accurate image was obtained even in the most difficult case 1.3 in which the inclusion was located in an area where the amplitude of the EM wave was much less compared with the one on the center line.

Actually, we had quite a large noise in our input data for the globally convergent method. This noise was generated by the following four factors: **(1)** Our governing PDE (1) cannot be derived from the Maxwell system. **(2)** Our theory does not work for our case when the coefficient ε_r has a discontinuity at the inclusion/background interface. Items 1 and 2 indicate that we have worked with a simplified mathematical model. **(3)** The experimental data itself naturally have a large noise. **(4)** We had an implicit noise in our follow up mathematical model occurred in the data pre-processing.

Thus, we believe that the accuracy of our results indicates robustness of the technique of [3, 4]. In summary, based on results of this publication, we conclude that the globally convergent numerical method of [3, 4] is now validated.

Acknowledgments

References

[1] Abramowitz M and Stegun A 1964 *Handbook of Mathematical Functions* (Washington, DC: National Bureau of Standards)

[2] Ammari H, Iakovleva E and Lesselier D 2007 Music-type electromagnetic imaging of a collection of small three dimensional inclusions *SIAM J. Sci.Comp.* **29** 674-709

[3] Beilina L and Klibanov M V 2008 A globally convergent numerical method for a coefficient inverse problem *SIAM J. Sci. Comp.* **31** 478-509

[4] Beilina L and Klibanov M V 2010 Synthesis of global convergence and adaptivity for a hyperbolic coefficient inverse problem *J. Inverse and Ill-Posed Problems* **18** issue 1

[5] Beilina L, Klibanov M V and Kokurin M Yu 2009 Adaptivity with relaxation for ill-posed problems and global convergence for a coefficient inverse problem. Preprint available on-line at *http://www.ma.utexas.edu/mp_arc* (posting date November 20, 2009) and at *http://www.math.chalmers.se/Math/Research/Preprints*, Chalmers Preprint Series, ISSN 1652-9715

[6] Beilina L and Klibanov M V 2009 A posteriori error estimates for the adaptivity technique for the Tikhonov functional and global convergence for a coefficient inverse problem. Preprint available on-line at *http://www.ma.utexas.edu/mp_arc* (posting date December 29, 2009) and at *http://www.math.chalmers.se/Math/Research/Preprints*, Chalmers Preprint Series, ISSN 1652-9715

[7] Beilina L, Samuelsson K and Åhlander K 2001 Efficiency of a hybrid method for the wave equation. In *International Conference on Finite Element Methods*, Gakuto International Series Mathematical Sciences and Applications. Gakkotosho CO., LTD

[8] Budak B M, Samarskii A A and Tikhonov A N 1988 *A Collection of Problems in Mathematical Physics* (New York: Dover Publications)

[9] Belishev M I 1997 Boundary control in reconstruction of manifolds and metrics (the bc method) *Inverse Problems* **13** R1-R45

[10] Belishev M I and Gotlib V Yu 1999 Dynamical variant of the bc-method: theory and numerical testing *J Inverse and Ill-Posed Problems* **7** 221-240

[11] Belkehir K and Saillard M 2005 Guest editors introduction. Testing inversion algorithms against experimental data: inhomogeneous targets *Inverse Problems* **21** issue 6 S1-S3

[12] Burov V A, Morozov S A and Rumyantseva O D 2002 Reconstruction of fine-scale structure of acoustical scatterers on large-scale contrast background, *Acoust. Imaging* **26** 231-238

[13] Cheney M and Isaacson D 1995 Inverse problems for a perturbed dissipative half-space *Inverse Problems* **11** 865-888

[14] Engl H W, Hanke M and Neubauer A 2000 *Regularization of Inverse Problems* (Boston: Kluwer Academic Publishers)

[15] Engquist B and Majda A 1977 Absorbing boundary conditions for the numerical simulation of waves *Math. Comp.* **31** 629-651

[16] Friedman A 1964 *Partial Differential Equations of Parabolic Type* (Englewood Cliffs, N.J.: Prentice Hall, Inc.)

[17] Gerrish H H Dugger W E Jr and Robert R M 2004 *Electricity and Electronics* (Merseyside, UK: Goodheart-Willcox Co. Inc.)

[18] Geffrin J M and Sabouroux P 2009 Continuing with the Fresnel database: experimental setup and improvements in 3D scattering measurements *Inverse Problems* **25** 042001

[19] Grinevich P G 2000 The scattering transform for the two-dimensional operator with a potential that decreases at infinity at fixed nonzero energy *Russ. Math. Surv.* **55** 3-70

[20] Kabanikhin S I, Satybaev A and Shishlenin M 2004 *Direct Methods of Solving Multidimensional Inverse Hyperbolic Problems*, (Utrecht, The Netherlands: VSP)

[21] Klibanov M V and A. Timonov A 2004 *Carleman Estimates for Coefficient Inverse Problems and Numerical Applications* (Utrecht, The Netherlands: VSP)

[22] Klibanov M V 1991 Inverse problems and Carleman estimates, *Inverse Problems* **8** 575–596

[23] Kuzhuget A V, Beilina L, Klibanov M V and Romanov V G 2010 The quasi-reversibility method for incomplete data collection and global convergence for a coefficient inverse problem, *in preparation*

[24] Ladyzhenskaya O A and Uralceva N N 1969 *Linear and Quasilinear Elliptic Equations* (New York: Academic Press)

[25] Ladyzhenskaya O A, Solonnikov V A and Uralceva N N 1968 *Linear and Quasilinear Equations of Parabolic Type* (Providence, R.I.: AMS)

[26] Lavrentiev M M, Romanov V G and Shishatskii S P 1986 *Ill-Posed Problems of Mathematical Physics and Analysis* (Providence, R.I.: AMS)

[27] Mueller J and Siltanen S 2003 Direct reconstructions of conductivities from boundary measurements *SIAM J. Sci. Comp.* **24** 1232-1266 1266

[28] Novikov R G 1988 Multidimensional inverse spectral problem for the equation $-\triangle\psi + (v(x) - Eu(x))\psi = 0$ *Functional Analysis and Its Applications* **22** 11-22

[29] Novikov R G 1992 The inverse scattering problem on a fixed energy level for the two-dimensional Schrodinger operator, *J. Func. Anal. and Its Applications* $\infty\prime\ni$ 409-463

[30] Reitz J R Milford F J and Christy R W 1980 *Foundations of Electromagnetic Theory* (Reading, Mass. : Addison-Wesley)

[31] Romanov V G 1986 *Inverse Problems of Mathematical Physics* (Utrecht, The Netherlands: VNU)

[32] Romanov V G 2009 On smoothness of a fundamental solution to a second order hyperbolic equation, *Siberian Math. J* **50** 700-705

[33] Special section on testing inversion algorithms against experimental data: inhomogeneous targets 2005 *Inverse Problems* **21** issue 6

[34] Special section on testing inversion algorithms against experimental data: 3D targets 2009 *Inverse Problems* *25* issue 2

[35] Tikhonov A N and Arsenin V Ya 1977 *Solutions of Ill-Posed Problems* (Washington, DC: Winston and Sons)

[36] Yamamoto M 2009 Carleman estimates for parabolic equations and applications Inverse Problems **25** 123013